Chemical Engineering Journal 520 (2025) 166135

Contents lists available at ScienceDirect

Chemical Engineering Journal

journal homepage: www.elsevier.com/locate/cej

High-yield ethanol production via thermocatalytic CO_2 hydrogenation over Cs/CuZnFe catalyst in a continuous flow reactor

Andrii Kostyniuk *, Blaž Likozar

Department of Catalysis and Chemical Reaction Engineering, National Institute of Chemistry, Hajdrihova 19, Ljubljana 1001, Slovenia

ARTICLE INFO

Keywords:
CO_2 hydrogenation
Cs/CuZnFe heterogeneous catalyst
C − C coupling
Ethanol synthesis

ABSTRACT

Achieving high ethanol yield and catalyst stability in CO_2 hydrogenation presents a significant scientific and technological challenge, which can be addressed through advanced catalyst design. Hence, in this work, we present the findings of our research on a Cs/CuZnFe active catalyst, which demonstrates effective and selective synthesis of C_{2+} alcohols (78.8 mol%) through CO_2 hydrogenation with corresponding conversion of 17.0 %. The optimized catalyst, denoted as 4%Cs/25%Cu − 25%Zn − 50%Fe, displays a remarkable space time yield (STY) of ethanol = 5.0 mmol·g_{cat}^{-1}·h^{-1} in the gas phase at 300 °C under 20 bar with $H_2/CO_2 = 3$ and GHSV = 9917 h^{-1}. The catalyst exhibits a high level of performance relative to most comparable systems in the literature. The exceptional catalytic activity is mainly due to the catalyst large pore diameter, significant crystallite size, excellent crystallinity, high oxygen vacancies, and low basicity. Additionally, the 4%Cs loading provides a stabilizing effect by preventing Cu loss and maintaining an optimal balance between low basicity and high oxygen vacancies, enhancing CO_2 activation while minimizing excessive adsorption and side product formation. Finally, our investigation into the mechanism reveals that the reaction follows a tandem pathway involving both CO insertion and the formate pathway, with the latter predominating.

1. Introduction

The rapid accumulation of greenhouse gases (GHGs), particularly CO_2 which accounts for approximately 72 % of total emissions, has become a major contributor to global warming [1]. This rise is largely driven by fossil fuel combustion, with global CO_2 emissions increasing from 33.9 billion tonnes in 2018 to 37.4 billion tonnes in 2024 [2,3]. To mitigate this trend, carbon capture and utilization (CCU) and carbon capture and storage (CCS) have emerged as critical approaches, with CCU being particularly attractive due to its potential to convert CO_2 into valuable chemicals [4]. Coupled with renewable H_2 from water electrolysis, CO_2 can be hydrogenated into a variety of products, including CO, CH_4, olefins, aromatics, dimethyl ether, and alcohols. Among these, ethanol is of special interest due to its role as a clean fuel and a versatile platform chemical. While ethanol can be produced via ethylene hydration or biomass fermentation, both routes have drawbacks related to cost, sustainability, and feedstock toxicity [5]. In contrast, direct CO_2 hydrogenation to ethanol offers a more sustainable and potentially scalable pathway [2,3,6–20].

Thermal catalysis, particularly over heterogeneous systems, has shown favorable kinetics and scalability over photocatalysis and electrocatalysis [21]. However, achieving high ethanol selectivity and productivity remains challenging. Noble-metal catalysts (Rh, Ru, Pd, Pt) have demonstrated good activity, yet their cost and limited scalability have driven the search for cheaper transition-metal-based alternatives, particularly Cu-based systems [22–26]. Cu is effective for methanol synthesis, but selectivity toward C_{2+} oxygenates requires the aid of promoters such as alkali metals, with Cs being the most effective (Cs > K > Na > Li) [27]. Recent studies have demonstrated the potential of Cs-promoted Cu–Fe–Zn systems for C_{2+} alcohol production. Xu et al. [28] reported 1.47 mmol g_{cat}^{-1} h^{-1} C_{2+} alcohol STY using a Cs–Cu–Fe–Zn catalyst, while Yang et al. [29] achieved 58.2 mg/mL_{cat}/h STY using pyridine-based ligands. Both studies highlighted the role of promoters in enhancing metal dispersion and electronic tuning. Wang et al. [30] further proposed a reaction mechanism involving Cs–Cu–ZnO synergy facilitating C—C coupling. Although these systems are promising, their STY values remain insufficient for industrial application. Silva et al. [31] explored steam-assisted CO_2 hydrogenation at atmospheric pressure but achieved limited productivity and stability. Li et al. [32] very recently developed an optimized 1Ni-4 K/Fe catalyst for CO_2 hydrogenation,

* Corresponding author.
E-mail address: andrii.kostyniuk@ki.si (A. Kostyniuk).

https://doi.org/10.1016/j.cej.2025.166135
Received 18 February 2025; Received in revised form 23 June 2025; Accepted 16 July 2025
Available online 19 July 2025

achieving a high STY_{C2+OH} of 317.0 mg/g/h with 21.1 % selectivity at 34.7 % CO_2 conversion, and demonstrating excellent catalytic stability over 300 h, highlighting its strong industrial potential. Despite these efforts, challenges persist in enhancing ethanol yield, selectivity, and catalyst stability. Therefore, developing novel, high-performing, and stable catalysts remains a critical goal for CO_2 valorization.

In this work, we report the direct hydrogenation of CO_2 to ethanol and higher alcohols (HA) using a series of xCs/CuZnFe catalysts. The study systematically investigates the effect of Cs loading, reaction temperature, and time-on-stream. Our optimized catalyst (4%Cs/CuZnFe) demonstrates one of the highest reported ethanol STY values (5.0 mmol g_{cat}^{-1} h^{-1}) among non-noble metal systems (Fig. 1 and Table S1). A comprehensive suite of characterization techniques, including BET (Brunauer-Emmett-Teller) surface area analysis, XRD (X-ray diffraction), XPS (X-ray photoelectron spectroscopy), CO_2-TPD (temperature-programmed desorption of CO_2), SEM (scanning electron microscopy), STEM (scanning transmission electron microscopy), EDX (energy-dispersive X-ray spectroscopy), ICP-OES (inductively coupled plasma optical emission spectroscopy) and in situ DRIFTS (diffuse reflectance infrared Fourier transform spectroscopy) study, were used to elucidate the catalyst structure, composition, and reaction mechanism. The results reveal that Cs incorporation plays a crucial role in modifying the catalyst surface, enhancing CO_2 activation, and facilitating C—C coupling via synergistic interactions among Cs, Cu, Zn, and Fe.

In contrast to previous study [28], our work investigates varying $CsNO_3$ loadings combined with markedly different Cu:Zn:Fe ratios, demonstrating that 4wt%Cs induces substantial structural and electronic changes in the CuZnFe catalyst. These changes are confirmed by XRD, BET, ICP-OES, SEM, and XPS revealing pronounced differences in crystallinity, porosity, and surface composition. Notably, our data show the presence of $CsNO_3$, which are not present or discussed in prior studies. Furthermore, our $CsNO_3$ introduction method results in observable redistribution of elements and strong interactions affecting the catalyst performance and stability.

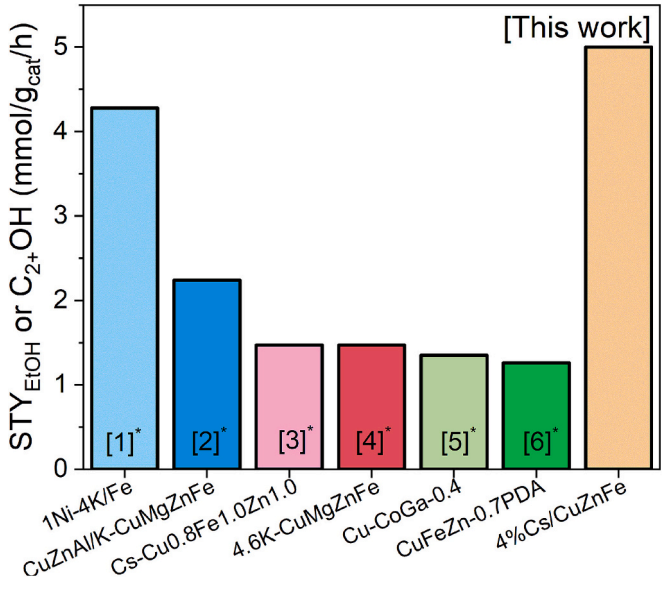

Fig. 1. Comparison of literature data with the most active catalyst in this study (4%Cs/CuZnFe). The numbers in the columns correspond to the cited references. *Indicates that the respective reference list is provided in the Supporting Information.

2. Experimental section

2.1. Chemicals used

Cesium nitrate ($CsNO_3$, 99 %), cupper nitrate ($Cu(NO_3)_2{\cdot}3H_2O$, 99 %), zinc nitrate ($Zn(NO_3)_2{\cdot}6H_2O$, 99 %), iron nitrate ($Fe(NO_3)_3{\cdot}9H_2O$, 99 %), ethanol (C_2H_5OH, >99.8 %), methanol (CH_3OH, >99.9 %), 1-propanol (C_3H_8O, 99.5 %), 2-propanol (C_3H_8O, 99.5 %), 1-butanol ($C_4H_{10}O$, 99.5 %), 2-butanol ($C_4H_{10}O$, 99.5 %), 3-methyl-1-butanol ($C_5H_{12}O$, ≥98.5 %), 1-pentanol ($C_5H_{12}O$, 99.5 %), acetone (C_3H_6O, >99.5 %), acetaldehyde (C_2H_4O, >99.5 %), acetic acid ($C_2H_4O_2$, >99.7 %), propanoic acid ($C_3H_6O_2$, >99 %), butanoic acid ($C_4H_8O_2$, >99 %), pentanoic acid ($C_5H_{10}O_2$, >99.5 %), and hexanoic acid ($C_6H_{12}O_2$, >99 %) were purchased from Merck.

2.2. Catalyst synthesis

2.2.1. Preparation of CuZnFe catalyst

Mixed CuZnFe oxide catalyst were prepared by using a coprecipitation method. In detail, the CuZnFe precipitates were obtained by a precipitation of Cu, Zn and Fe nitrate solution (0.2 mol/L) using aqueous $(NH_4)_2CO_3$ (0.24 mol/L) as the precipitating agent with a single-drop method at 70 °C and pH = 9 under stirring where Fe should always be added first, followed by Cu, then Zn. The molar ratio of Cu:Zn:Fe was set at 1:1:2. The products were collected by centrifugation and washed with deionized water for several times, followed by drying at 80 °C for 12 h. After calcination at 400 °C for 2 h, the CuZnFe ternary metal oxides were obtained.

2.2.2. Preparation of CuZnFe/ZSM-5 catalyst

H-ZSM-5 commercial zeolite powder (molar SiO_2/Al_2O_3 = 30, Zeolyst Int., CBV 3024E) was pretreated at 550 °C for 6 h in an air followed by cooling down to room temperature before being impregnated. Preparation of the 10wt%Cu − 10wt%Zn − 20wt%Fe/ZSM-5 catalyst involved the impregnation of zeolite using the wet impregnation method. For a typical synthesis, the experimentally desired amount of $Fe(NO_3)_3{\cdot}9H_2O$, $Zn(NO_3)_2{\cdot}6H_2O$ and $Cu(NO_3)_2{\cdot}3H_2O$ were dissolved in the corresponding volume of distillate water for obtaining 0.05–0.1 M solutions. The solutions were stirred at 50 °C for 30 min. Next, the solutions of $Cu(NO_3)_2{\cdot}3H_2O$ were added to the H-ZSM-5 zeolite for 1 h. Thereafter, $Zn(NO_3)_2{\cdot}6H_2O$ was added to the mixture and stirred for 1 h. Finally, $Fe(NO_3)_3{\cdot}9H_2O$ was added with vigorous stirring for 1–2 h at 80 °C. After impregnation, all samples were dried overnight at 110 °C. Afterward, they were calcined for 6 h at 550 °C in an air atmosphere. All catalysts were reduced in flow of H_2 for 1 h. The CuZnFe/ZSM-5 catalyst was included as a reference, given the extensive use of zeolite-supported metal catalysts in CO_2 hydrogenation studies and the widespread application of wet impregnation as a straightforward and representative preparation method in the literature. While we recognize that the difference in preparation method limits direct comparison, our intent was to provide a relevant benchmark for researchers exploring zeolite-supported systems.

2.2.3. Preparation of xCs/CuZnFe

To synthesize *x*%Cs/CuZnFe, the procedure involved mixing powdered CuZnFe catalyst with $CsNO_3$ salt. The CuZnFe precursor was prepared using the same co-precipitation method described in Section 2.2.1 for all catalyst samples. The $CsNO_3$ salt was dissolved in deionized water to create a 0.2 M solution, which was then heated to 70 °C and combined with the powdered catalyst. After 2 h, the mixture was left to dry overnight at 110 °C. Following the drying process, the catalyst was subjected to calcination in a furnace at 400 °C for a duration of 2 h. Before commencing the reaction, all catalysts underwent a reduction process in a flow of hydrogen for a duration of 1 h.

2.3. Catalyst characterization

Textural properties of the catalysts were measured by the N_2 adsorption-desorption method on a Micromeritics ASAP 2020 instrument. Before the experiment, the sample (150 mg) was degassed at 200 °C overnight (temperature ramp 10 °C/min) under vacuum (10^{-3} Pa), and afterward, an N_2 adsorption-desorption analysis was carried out at −196 °C, while the pore-size distribution was calculated based on the desorption isotherms by the Barrett–Joyner–Halenda (BJH) method and the total surface area was calculated by the Brunauer–Emmett–Teller (BET) method.

The solid phase catalysts composition was identified by powder X-ray diffraction analysis on PANalytical XpertPro instrument using CuKα1 radiation (1.54056 Å) in the range of 2 theta angles ranging from 10° to 70° with increments of 0.034°. The average crystallite size was calculated using the Scherrer equation, based on the most significant peaks at 33.4°, 35.6°, 36.3°, 38.9°, 54.1°, and 62.9°. The relative crystallinity percentage (*RC%*) within the 2θ range of 10–70° was calculated using the formula: $RC\% = Ic/(Ic + Ia)$, where *Ic* represents the total intensity of the crystalline peaks, and *Ia* represents the total intensity of the amorphous peaks [33]. Additionally, the *RC%* was calculated relative to the CuZnFe catalyst using the following equation: $RC\% = Ic_{(xCs/CuZnFe)}/(Ic_{(CuZnFe)} + Ia_{(CuZnFe)})$, where $Ic_{(xCs/CuZnFe)}$ is the crystalline intensity of the Cs sample divided by the total intensity of the crystalline and amorphous peaks of the CuZnFe catalyst.

The element content was determined by inductively coupled plasma mass spectroscopy (ICP − OES) using an Agilent 7500ce. Before the analysis, the samples were fumed with a mixture of HF and $HClO_4$. The residue was dissolved in the mixture of HCl and H_3BO_4 and diluted for determination of the Cs content in catalyst samples. The amount of carbon in the studied spent catalysts was quantified using TGA − FTIR (thermogravimetric analysis-infrared spectrometry) Spectrum 3 with EGA 4000 from PerkinElmer. The analysis of the spent catalysts was performed in the temperature range from 40 to 750 °C with a heating rate of 10 °C/min in an air stream with a flow rate of 100 mL/min.

A scanning electron microscope (FE–SEM SUPRA 35–F, Carl Zeiss) equipped with an energy-dispersive spectrometer Inca 400 (Oxford Instruments) was used to record the morphology of the studied catalysts, while the particle size of each sample was calculated from the obtained HRSEM images using the ImageJ software. STEM micrographs and EDXS chemical mapping of the samples were obtained using a JEOL ARM 200 CF microscope with a cold field-emission gun and Jeol Centurio EDXS system. More detailed experimental procedures for STEM–EDX analysis have been described in our previous work [34].

CO_2 temperature-programmed desorption (CO_2-TPD) experiments were carried out on Microtrac MRB BELCAT instrument as follows: 0.1 g sample was reduced under 5 %H_2/Ar atmosphere (30 mL/min) at 350 °C for 1 h. Then, the gas was switched to He at a flow rate of 30 mL/min for 1 h to purge the residual H_2 and cooled down to 50 °C. Then, samples were exposed to a flow of CO_2 (10%CO_2 with He as a balance gas) in 30 mL/min flow at 50 °C for 30 min, the gas was switched to He at a flow rate of 30 mL·min^{-1} to purge the residual CO_2. The TPD measurements were conducted by using He as carrier from 50 to 700 °C and CO_2 was detected by a thermal conductivity (TCD) detector. At the same time, a mass spectrometer detector was employed to confirm the absence of water in the samples, detecting the characteristic $m/z = 44$ fragment. This analysis was conducted using an online Pfeiffer Vacuum Thermostar quadrupole mass spectrometer.

The X-ray photoelectron spectroscopy (XPS) analyses were conducted using the PHI-TFA XPS spectrometer manufactured by Physical Electronics Inc., equipped with an Al-monochromatic source emitting photons at an energy level of 1486.6 eV. The examined area had a diameter of 0.4 mm. Quantification of surface composition was determined from XPS peak intensities, taking into consideration the relative sensitivity factors provided by the instrument manufacturer. The surface sensitivity was in the range of 2–5 nm. All data underwent correction based on the binding energy of C 1 s (284.8 eV) adventitious carbon. The accuracy of binding energy measurement was within ±0.3 eV [34].

The in situ DRIFTS analysis was performed using a PerkinElmer Spectrum 100 FT-IR spectrometer, which was equipped with a Harrick reaction chamber and a mercury cadmium telluride (MCT) detector. Spectral data were collected in the 800–4000 cm^{-1} range at a resolution of 4 cm^{-1}, with each measurement based on an average of eight scans. Before recording the spectra, the catalyst sample underwent a reduction treatment at 300 °C for 1 h under a H_2 flow of 30 mL/min. Following this, background spectra were acquired by averaging eight scans at the same resolution, once the system had cooled to the target temperature under continuous H_2 flow. The DRIFTS measurements were then conducted at temperatures between 25 and 300 °C, using a gas mixture of H_2 and CO_2 in a 3:1 ratio (total flow rate: 30 mL/min) at a pressure of 20 bar. Temperature control of the sample was maintained using an internal thermocouple.

2.4. Catalytic evaluation

The catalysts were tested in powdered form (0.25 g), inserted with quartz wool in a custom-designed parallel packed bed reactor unit using a 6.35 mm tube (Fig. S1). The gas line from the reactor was connected to a gas chromatograph (micro-GC, Agilent 490), equipped with TCD detector and CP-Molsieve and PoraPlot U column. The gasses used for testing and reduction were H_2 (5.0, Messer) and CO_2 (4.5, Messer) with a ratio of $H_2/CO_2 = 3$. The catalyst was reduced prior to the reaction in H_2 in atmospheric pressure at 300 °C for 1 h. The gas reaction mixture was provided via H_2 and CO_2 cylinders, mixed before the reactor inlet. The gas feed was at GHSV = 9917 h^{-1}, reactor feed was set at (0.03 g/min or 60 mL/min) and the reaction pressure was 20 bar. The temperature program for the catalytic testing in the reactor was set at 200 °C for 8 h, 250 °C at 5 h and 300 °C at 6 h, with 30 min of heating between ramps. The major gas-phase products included ethanol and C_{2+} alcohols, in addition to CO, CH_4, methanol and unreacted CO_2 and H_2. The presence of alcohols in the gas phase was confirmed through retention time matching with standard compounds and quantitative calibration.

In addition, liquid-phase products were collected at the end of each catalytic run (after 16–19 h) via condensation and analyzed offline using a FOCUS Thermo Scientific GC instrument equipped with a flame ionization detector (FID) and a DB-WAX Ultra Inert capillary column. Product identification was performed using an Agilent 7890 A GC system coupled with a 5977B mass selective detector (GC–MS), also equipped with a DB-WAX Ultra Inert capillary column, which had dimensions of 30 m in length, an internal diameter of 0.25 mm, and a film thickness of 0.25 μm. The identification and quantification of these liquid products were performed through the utilization of an external calibration technique within the 0.01–5 wt% range, employing the chemicals referenced in the chemical section. The prominent liquid products identified included ethanol, 1-propanol, 1-pentanol, 1-butanol, and methanol. The GC–MS analysis also revealed traces of liquid byproducts, which included acetone, 2-butanol, 3-methyl-1-butanol, propanoic acid, butanoic acid, acetic acid, pentanoic acid, hexanoic acid, and acetaldehyde. The relative errors in the measured product concentrations were found to be <5 %. The carbon balance was always higher than 95 %.

The total conversion of CO_2 (X_{CO2}), was calculated using the next equation:

$$X_{CO2}(\text{mol}\%) = \frac{n(CO2)_{in} - n(CO2)_{out}}{n(CO2)_{in}} \times 100\% \quad (1)$$

where $n(CO_2)_{in}$ and $n(CO_2)_{out}$ are the input and output moles of CO_2 before and after the reaction, respectively. The carbon product selectivity, $S(C_i)$, (excluding CO fraction) was calculated using the equation below [24,35]:

$$S(C_i)(mol\%) = \frac{mol(P_i) \times C_n}{\sum mol(P_i) \times C_n - n(CO)out} \times 100\% \quad (2)$$

$n(P_i)$ and C_n are specified reaction product and carbon number, respectively. The values in this article are in mol percent.

While CO fraction was calculated accordingly [36]:

$$S_{CO}(mol\%) = \frac{n(CO)_{out}}{\sum mol(P_i) \times C_n} \times 100\% \quad (3)$$

The total mass balance was always higher than 98 %. The space time yield (STY) was calculated as following eq. (4), where the n_i represent the number moles of product (ethanol and/or C_{2+} alcohols), m_{cat} represents the mass of catalysts (g), t represents the reaction time (h).

$$STY\ (mmol \bullet g_{cat}^{-1} \bullet h^{-1}) = \frac{n_i}{(m_{cat} \bullet t)} \bullet 1000 \quad (4)$$

Gas hourly space velocity (GHSV) was calculated as follow, where FR is the volumetric flow rate of the gas mixture of H_2 and CO_2 at STP, mL/h; and V_{cat} is the volume of the catalyst bed, ml.

$$GHSV_{total}\ (h^{-1}) = \frac{FR\left(\frac{mL}{h}\right)}{V_{cat}(mL)} \quad (5)$$

The carbon balance (CB) was calculated according to the following:

$$CB = \frac{n(CO2)_{out} + n(CO)_{out} + \sum mol(P_i) \times C_n}{n(CO2)_{in}} \quad (6)$$

3. Results and discussion

3.1. Catalyst characterizations

Fig. 2 shows the N_2 adsorption-desorption curves and pore size distribution. The N_2 adsorption-desorption isotherms of the CuZnFe and *x*Cs/CuZnFe catalysts exhibit typical type IV behavior with distinct hysteresis loops, indicative of mesoporous structures and variations in pore geometry and connectivity [37]. The volume of N_2 adsorbed varies significantly among the different catalysts. Specifically, the CuZnFe and 4%Cs/CuZnFe catalysts exhibit type IV isotherms with H3-type hysteresis loops, which are typically associated with slit-like pores and aggregates of plate-like particles. These samples show relatively low N_2 uptake, indicating lower specific surface area. This is consistent with the ICP-OES results, which confirm that both of these samples contain the highest Cu content in the series. The higher Cu loading may lead to partial pore blockage or denser packing of surface particles, which can reduce the accessible pore volume and surface area, despite the presence of mesoporosity.

In contrast, the 2 %Cs/CuZnFe catalyst exhibits a type IV isotherm with a broader H1-H3 mixed hysteresis loop. This sample shows the highest N_2 uptake and BET surface area (60.9 m^2/g), indicating that low Cs loading enhances surface texture and pore accessibility. The incorporation of a small amount of Cs may lead to better dispersion of metal oxides and reduced particle aggregation, resulting in the formation of additional mesopores or the exposure of previously inaccessible ones. The 8%Cs/CuZnFe catalyst also follows a type IV isotherm, but with a slightly different profile and a more pronounced H3-type hysteresis loop. This suggests a combination of mesopores and larger interparticle voids, possibly due to the aggregation of $CsNO_3$ domains at higher Cs loadings. While this sample shows a higher N_2 uptake compared to the undoped CuZnFe, its surface area is still lower than that of the 2 %Cs/CuZnFe, reflecting a more complex interaction between excessive Cs coverage and pore structure. These differences in adsorption behavior and isotherm shape are closely linked to both the structural role of Cs and the compositional effects observed across the series.

The BJH pore size distribution curves further elucidate the mesoporous nature of the catalysts and the impact of Cs doping. The CuZnFe catalyst displays a peak pore diameter (PD) around 35 Å with broad pore size distributions, suggesting a range of pore sizes contributing to the overall porosity. The 2 %Cs/CuZnFe catalyst shows a shift in the pore size distribution with a peak PD around 54 Å, and the distribution is narrower, indicating more uniform pore sizes compared to the base catalyst. The 4%Cs/CuZnFe catalyst's pore size distribution is similar to the base catalyst, with peak diameters around 35 Å, and it also has a broad pore size distributions. The 8%Cs/CuZnFe catalyst exhibits an increase in peak PD to around 59 Å, similar to the 4%Cs/CuZnFe sample, with the distribution remaining narrow, suggesting a consistent mesoporous structure at higher Cs content.

The elemental composition and structural properties of the CuZnFe and *x*Cs/CuZnFe catalysts provided in Table 1 offer additional insights. ICP-OES analysis revealed a reduction in Cu content specifically in the 2 %Cs/CuZnFe and 8%Cs/CuZnFe samples. The observed leaching of Cu in these samples, but not in the 4%Cs/CuZnFe sample, may be attributed to an optimal stabilizing effect achieved at the 4%Cs loading, which is also consistent with the XRD and XPS analyses. At this concentration, the $CsNO_3$ may create a more balanced interaction with the CuZnFe catalyst matrix, effectively anchoring Cu species to the support and reducing their mobility. This stabilization minimizes the likelihood of Cu dissolution, potentially resulting in lower leaching rates. In contrast, the lower 2 %Cs loading might not provide sufficient coverage or interaction strength to protect Cu, leaving some Cu particles more exposed and susceptible to leaching. Similarly, the higher 8%Cs loading may induce an imbalance by oversaturating the surface or causing uneven Cs distribution, which could disrupt the Cu-support interactions and increase the vulnerability of Cu to leaching. The 4%Cs loading may also achieve a more uniform distribution on the support surface, which

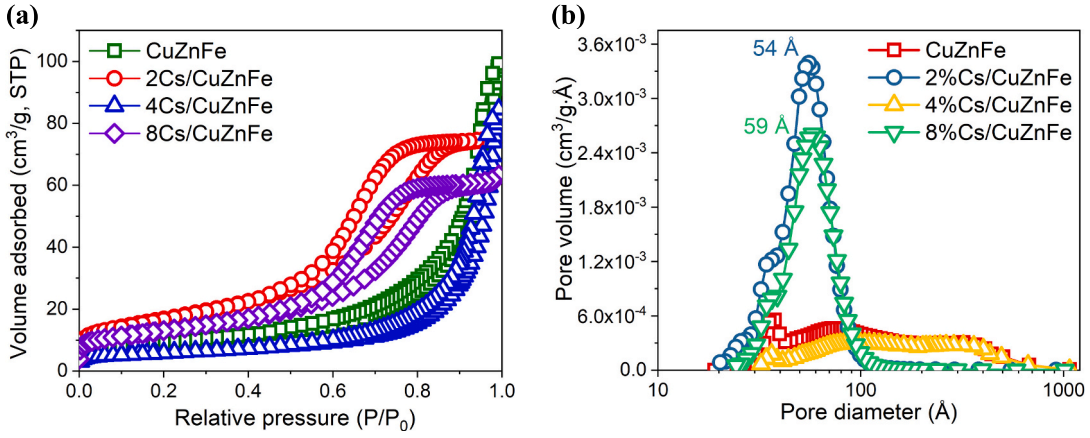

Fig. 2. N_2 adsorption-desorption isotherms (a) and BJH pore size distribution (b) of the CuZnFe and *x*Cs/CuZnFe catalysts.

Table 1
Elemental composition and structural properties of the CuZnFe and *x*Cs/CuZnFe catalysts.

Catalyst	Cs[a] (wt %)	Cu[a] (wt %)	Zn[a] (wt %)	Fe[a] (wt %)	S_{BET}[b] (m^2/g)	S_{micro}[b] (m^2/g)	S_{meso}[b] (m^2/g)	V_{micro}[c] (cm^3/g)	V_{total}[f] (cm^3/g)	V_{meso}[c] (cm^3/g)	PD[d] (nm)	Crystallite size[e] (nm)	RC[e] (%)	RC vs CuZnFe[e] (%)
CuZnFe	–	19	21	41	31.7	1.9	29.8	$7.6{\cdot}10^{-4}$	0.149	0.148	15.5	20.6	96.5	96.5
2%Cs/CuZnFe	2.0	13	21	43	60.9	1.9	59.0	$4.3{\cdot}10^{-4}$	0.117	0.116	5.4	19.0	87.9	64.3
4%Cs/CuZnFe	3.0	18	19	39	20.5	4.4	16.1	$2.2{\cdot}10^{-3}$	0.126	0.124	19.2	22.0	97.1	108.6
8%Cs/CuZnFe	6.0	12	20	40	46.3	4.8	41.5	$2.2{\cdot}10^{-3}$	0.096	0.094	5.9	18.1	91.4	67.2

[a] ICP – OES.
[b] BET method.
[c] t-plot method.
[d] Average pore diameter (PD) measured from the desorption branch according to the BJH method.
[e] The crystallite size and relative crystallinity (RC) were obtained and calculated from XRD data.

enhances the stabilization of Cu by reducing its exposure and preventing leaching. This contrasts with the 2 %Cs, where insufficient Cs coverage may leave exposed Cu regions prone to dissolution, and the 8%Cs, where excess Cs may lead to clustering or surface modification that destabilizes Cu. Additionally, the 4%Cs concentration may create an ideal modification of the support's basicity or surface chemistry, which could further help anchor Cu. In contrast, the lower Cs content may not adequately adjust these properties, while the higher Cs concentration could alter the surface to an extent that promotes Cu solubilization. The surface area (S_{BET}) and mesoporous surface area (S_{meso}) increase significantly with the addition of Cs, particularly in the 2 %Cs/CuZnFe sample, which has the highest S_{BET} of 60.9 m^2/g and S_{meso} of 59.0 m^2/g. This indicates that even a small amount of Cs significantly enhances the surface area. However, a further increase in Cs content to 4 % and 8 % results in a reduction of S_{BET} and S_{meso}. The notable increase in specific surface area and corresponding decrease in average pore diameter for the 2 %Cs/CuZnFe sample may be attributed to the partial dispersion of $CsNO_3$ over the surface of the catalyst support at this lower loading. At 2 wt%, Cs is likely distributed more finely and uniformly across the surface without forming larger aggregates or blocking pores. This dispersion may lead to surface cleaning effects or modifications that expose previously inaccessible micropores or smaller mesopores, resulting in an apparent increase in total surface area and a shift toward smaller average pore sizes. In contrast, higher Cs loadings (e.g., 4 % and 8 %) may lead to partial pore blockage or the formation of larger Cs-containing domains, which could reduce the available surface area and shift the pore size distribution in the opposite direction.

The pore volumes (V_{total} and V_{meso}) show a similar trend. The CuZnFe catalyst has V_{total} of 0.149 cm^3/g and V_{meso} of 0.148 cm^3/g. The 2 %Cs/CuZnFe sample has slightly lower V_{total} and V_{meso} values of 0.117 cm^3/g and 0.116 cm^3/g, respectively. The 4%Cs/CuZnFe catalyst show increases in V_{total} and V_{meso}, indicating that higher Cs content increases the overall pore volume. However, the 8%Cs/CuZnFe sample has the lowest V_{total} (0.096 cm^3/g) and V_{meso} (0.094 cm^3/g) compared to the other samples, suggesting that an excess of $CsNO_3$ leads to a reduction in pore volume. The average PD measured by the BJH method reveals that the CuZnFe catalyst has a PD of 15.5 nm, while the 2 %Cs/CuZnFe catalyst has a significantly smaller PD of 5.4 nm. The 4%Cs/CuZnFe catalyst shows a larger PD of 19.2 nm, and the 8%Cs/CuZnFe catalyst has a PD of 5.9 nm. This variation in PD with different Cs content indicates that Cs doping not only affects the surface area and pore volume but also the pore size distribution, with the 4%Cs/CuZnFe catalyst exhibiting the largest pores. Although the 4%Cs catalyst exhibited a relatively low surface area and moderate pore volume, its notably larger average PD may aid in improving mass transport, potentially contributing to enhanced ethanol selectivity. Nevertheless, further diffusion and kinetic studies would be necessary to confirm this hypothesis.

The XRD patterns for the synthesized samples of CuZnFe, 2 %Cs/CuZnFe, 4%Cs/CuZnFe, and 8%Cs/CuZnFe reveal distinct crystalline phases, including ZnO, CuO, Fe_2O_3, and $CsNO_3$ (Fig. 3). The presence of ZnO is confirmed by peaks at 2θ values of 31.8°, 34.5°, 36.3°, 47.6°, 56.7°, 62.9°, 66.4°, and 68.0° (COD No. 96–900-4182), while CuO peaks are observed at 35.6°, 38.9°, 48.4°, 58.4°, 61.7°, 66.4°, and 68.0° (COD No. 96–901-6327). Fe_2O_3 is identified by peaks at 24.2°, 33.3°, 35.6°, 40.9°, 49.6°, 54.1°, 62.5°, and 63.9° (COD No. 96–154-6384), and $CsNO_3$ by peaks at 19.9°, 28.3°, and 45.5° (COD No. 96–200-1972). Calcination at 400 °C for 2 h in static air may not ensure complete $CsNO_3$ decomposition, particularly when it is highly dispersed or partially stabilized by the support, as evidenced by XRD patterns (Fig. 3) showing crystalline $CsNO_3$ domains in the 2 %, 4 %, and especially 8%Cs samples. $CsNO_3$ melts in the range of 404 to 411 °C but decomposes over a broad temperature range from 450 to 750 °C, producing NO_2 and N_2O as by-products [38,39]. According to the literature [40], complete decomposition of $CsNO_3$ occurs only after multiple heat treatment cycles, such as ten repetitions of 20 h of calcination at 525 °C, which explains the presence of residual crystalline $CsNO_3$ in the calcined

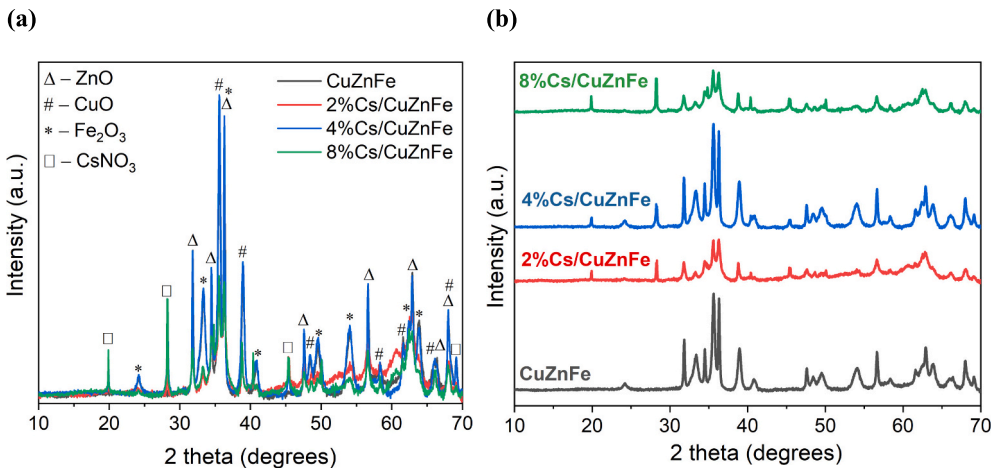

Fig. 3. XRD patterns of the CuZnFe and *x*Cs/CuZnFe catalysts.

catalysts.

The structural and compositional analysis of the CuZnFe and *x*Cs/CuZnFe catalysts, as summarized in Table 1, reveals significant insights into the influence of Cs loading on the crystallite size and relative crystallinity (RC) of the catalyst components. The crystallite size and RC values were derived from XRD data, providing a direct correlation between the Cs content and the structural properties of the catalysts. The base CuZnFe catalyst exhibited well-defined peaks corresponding to ZnO, CuO, and Fe_2O_3, indicating a relatively crystalline structure without the presence of $CsNO_3$. This is reflected in the crystallite size of 20.6 nm and high RC values (96.5 %), which suggest a stable and ordered crystalline phase. Upon introducing Cs into the CuZnFe system, significant changes in both crystallite size and RC were observed. The 2 %Cs/CuZnFe catalyst shows a slight reduction in crystallite size to 19.0 nm, accompanied by a decrease in the RC (64.3 %) of CuO, ZnO, and Fe_2O_3, particularly in comparison to the CuZnFe catalyst. This suggests that even a small amount of Cs leads to structural alterations, possibly due to the partial incorporation of Cs into the metal oxide matrix, disrupting the crystalline order. The 4%Cs/CuZnFe catalyst demonstrates an increase in crystallite size to 22.0 nm and a significant rise in the RC values, surpassing those of the base CuZnFe catalyst. This increase is particularly notable in the CuO, ZnO, and Fe_2O_3 phases, which suggests that Cs not only enhances the crystallization of these oxides but also promotes the formation of more ordered crystalline structures. The appearance of more intense $CsNO_3$ peaks in the XRD pattern supports this, indicating that Cs acts as a flux, aiding in the growth of well-defined crystalline domains. At the highest Cs loading of 8 %, the crystallite size decreases to 18.1 nm, accompanied by a broadening of the diffraction peaks for CuO, ZnO, and Fe_2O_3, as well as more prominent $CsNO_3$ peaks. This broadening indicates increased lattice strain or reduced crystallite size, likely due to the further incorporation of Cs into the metal oxide lattice, disrupting the crystalline order. The reduction in RC for the metal oxides compared to the 4%Cs/CuZnFe sample further corroborates this disruption, suggesting that beyond a certain threshold, Cs incorporation leads to a deterioration in the crystalline structure. These observations underscore the dual role of Cs in modifying the structural properties of the CuZnFe catalyst. At moderate Cs levels (4 %), the enhancement in crystallinity and crystallite size suggests improved structural integrity, which enhanced catalytic performance. However, at higher Cs levels (8 %), the disruption of crystallinity affected catalytic activity adversely, indicating an optimal Cs loading around 4 % for achieving the best balance between crystallite size, crystallinity, and catalytic performance.

The SEM images present morphological comparisons between the CuZnFe catalyst and the 4%Cs/CuZnFe catalyst (Fig. 4). The CuZnFe catalyst exhibits a relatively uniform distribution of particles with a

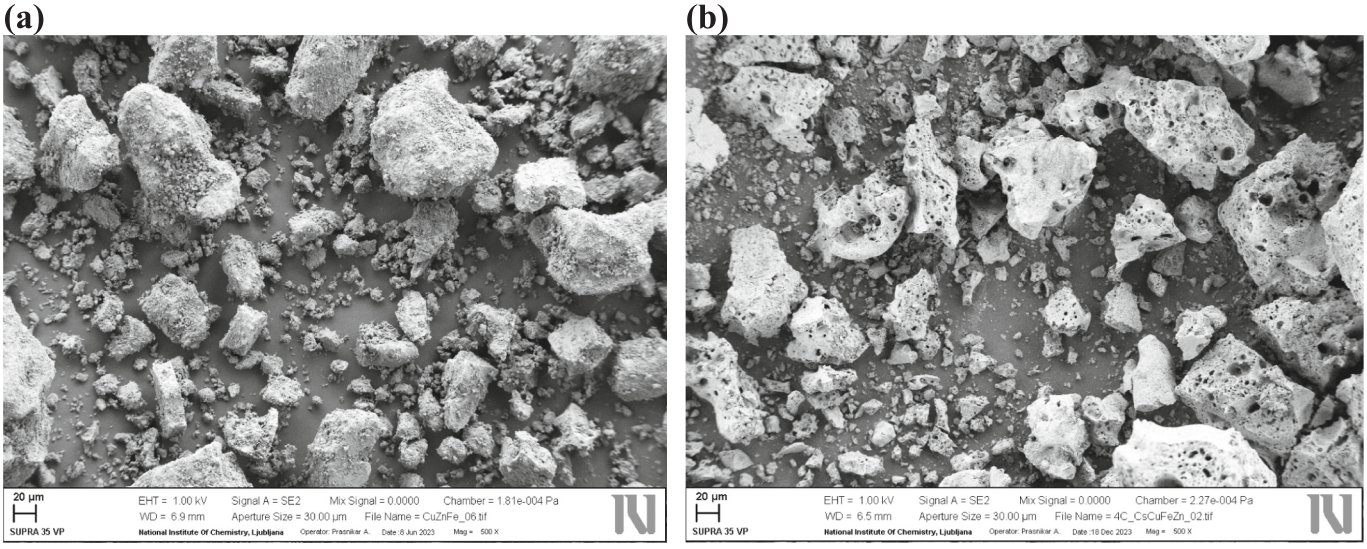

Fig. 4. SEM scans of CuZnFe – (a) and 4%Cs/CuZnFe samples – (b).

range of sizes. The particles appear to be somewhat aggregated, forming larger clusters with irregular shapes. The surface texture is rough, indicating a relatively high degree of surface area which is beneficial for catalytic activity. The 4%Cs/CuZnFe catalyst shows (Fig. 4b) significant morphological changes compared to the CuZnFe catalyst. The particles are more porous and less aggregated, with a distinct sponge-like structure. This indicates that the incorporation of Cs has led to the formation of a more open and porous structure. The increased porosity is beneficial as it can enhance the accessibility of reactants to the active sites of the catalyst, potentially improving catalytic performance. Additionally, the surface of the particles appears smoother compared to the CuZnFe catalyst, reflecting morphological differences induced by Cs addition, although this may not directly influence catalyst−reactant interactions.

Table S2 provides the SEM-EDX analysis data for the CuZnFe and xCs/CuZnFe catalysts, showing the elemental composition in terms of weight percentage (wt%). The SEM-EDX analysis reveals the compositional changes that occur with the incorporation of Cs into the CuZnFe catalyst matrix. For the CuZnFe catalyst, the composition remains consistent across different scans, indicating a homogeneous distribution of elements. The high Fe content (35.6 wt%) and significant amounts of Cu (20.1 wt%), O (29.7 wt%), and Zn (14.6 wt%) suggest the formation of a stable catalyst matrix. In the 2 %Cs/CuZnFe catalyst, the presence of Cs at an average of 4.0 wt% introduces noticeable changes. The Cu content decreases to 13.7 wt%, while Fe increases to 39.1 wt%, and Zn to 20.2 wt%. The decrease in O content to 23.1 wt% indicates that Cs incorporation affects the oxygenated species in the catalyst. The variations in Cs content across scans (3.5 to 4.7 wt%) suggest that Cs distribution may be slightly heterogeneous at this doping level. The 4%Cs/CuZnFe catalyst shows an average Cs content of 3.8 wt%, similar to the 2 % sample, but with slight variations in the distribution. The Cu content returns to around 20.1 wt%, close to the undoped sample, while Fe and O contents are 34.6 and 27.2 wt%, respectively. The Zn content decreases slightly to 14.4 wt%. These changes suggest that the addition of Cs at this level leads to a redistribution of the elements within the catalyst, potentially impacting the catalyst structural and functional properties. The 8%Cs/CuZnFe catalyst exhibits the highest Cs content at 8.7 wt%, with Cu content decreasing further to 13.3 wt%. Fe remains consistent at 34.6 wt%, while O and Zn contents are 23.5 and 20.0 wt%, respectively. The increased Cs content significantly impacts the elemental composition, with variations across different scans indicating a more heterogeneous distribution of Cs. This high level of Cs incorporation likely induces substantial structural changes in the catalyst matrix, which could influence its catalytic behavior and performance. The elemental compositions from SEM-EDX, combined with the structural properties from BET and BJH analyses, provide a comprehensive understanding of how Cs incorporation affects the CuZnFe catalysts. The changes in surface area, pore volume, and pore size distribution correlate with the variations in elemental composition, highlighting the intricate relationship between composition, structure, and catalytic properties. Taken together with the catalytic data, the SEM and SEM-EDX results demonstrate a strong correlation between morphology, composition, and catalytic behavior, directly supporting our structure-activity discussion.

Fig. S2a and Fig. S2b present the scanning transmission electron microscopy bright-field (STEM-BF) images of the CuZnFe and 4%Cs/CuZnFe catalysts, respectively. These images provide insights into the morphology and structural characteristics of the catalysts at the nanoscale. In Fig. S2a, the STEM-BF image of the CuZnFe sample reveals a heterogeneous distribution of particles with varying sizes. The particles appear to be agglomerated, forming clusters with indistinct boundaries. The average particle size is difficult to ascertain precisely due to the agglomeration, but it appears to be in the range of 10–30 nm. The introduction of 4%Cs does not significantly influence the particle morphology (Fig. S2b). The particles in this sample remain within the same size range, although they exhibit slightly clearer boundaries. Both samples shown in Fig. S2 contain numerous particles, which are densely packed, forming abundant mesopores [28]. Fig. 5a and Fig. 5b present the STEM images and EDX elemental mappings of the CuZnFe and 4% Cs/CuZnFe catalysts, respectively. These analyses provide valuable information on the elemental distribution and homogeneity within the catalyst samples. In Fig. 5a, the STEM image of the CuZnFe sample, coupled with the EDX mappings, shows the distribution of O, Cu, Zn, and Fe within the catalyst. The EDX mappings indicate a relatively uniform distribution of these elements throughout the sample. The Cu, Zn, and Fe signals are well-dispersed, suggesting a homogeneous composition. The presence of oxygen is also uniform, indicating that the metal oxides are evenly distributed. The addition of 4%Cs is clearly evident in the EDX mapping (Fig. 5b). The elemental distribution of Cu, Zn, Fe, and O remains relatively uniform, similar to the CuZnFe sample. At the same time, the Cs signal shows a distinct distribution, indicating successful incorporation of Cs into the catalyst structure.

However, we acknowledge that one localized region on the lower-left side of the particle exhibits a slightly higher intensity of both Cu and O signals, suggesting the presence of a CuO-rich domain (Fig. 5a). This observation is consistent with our XRD data (Fig. 3), which confirms the presence of crystalline CuO based on distinct diffraction peaks. The coexistence of well-dispersed Cu with a minor localized CuO-rich region suggests that while the catalyst is overall compositionally homogeneous, some CuO domains may form during calcination, especially in areas with slightly higher Cu concentration. This local inhomogeneity is likely due to phase segregation during synthesis and heat treatment, which can occur in multicomponent oxide systems. Nonetheless, the limited extent and small size of the CuO-rich area observed in the STEM-EDX do not significantly compromise the catalyst overall uniformity. We have revised the manuscript to acknowledge this observation and to clarify that while CuO is confirmed as a phase, it remains largely dispersed with only minor localized enrichment, consistent with both

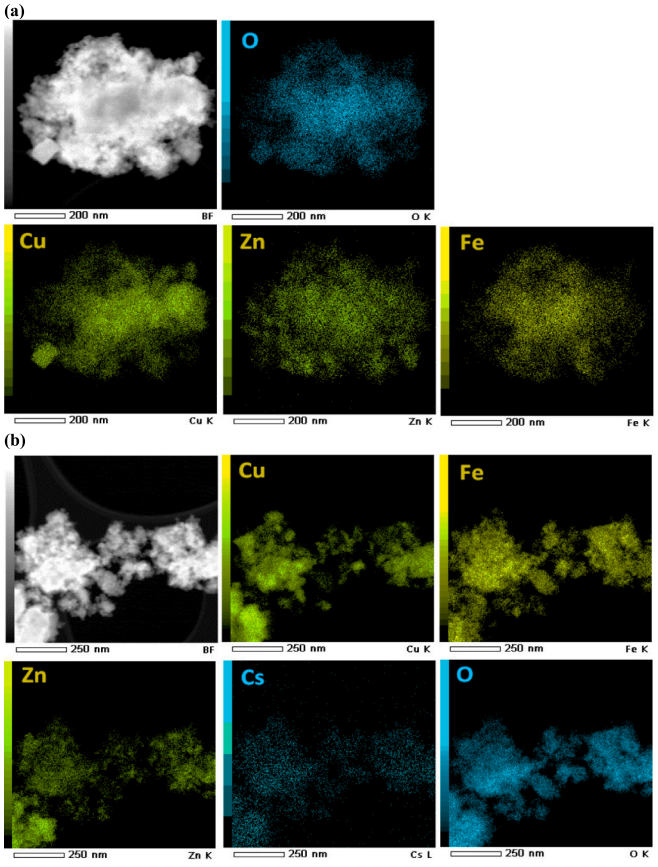

Fig. 5. STEM images and EDX elemental mappings of CuZnFe – (a) and 4%Cs/CuZnFe – (b) samples.

STEM-EDX and XRD findings.

The presence of Cs appears to be well-integrated with the other elements, suggesting that the addition of Cs does not disrupt the overall homogeneity of the catalyst but rather enhances it. These observations are significant for understanding the catalytic performance. The homogeneous distribution of elements suggests that the active sites are uniformly available, which is beneficial for catalytic reactions. The incorporation of Cs enhances the structural properties without disrupting the uniformity, potentially leading to improved catalytic activity and selectivity in CO_2 hydrogenation reaction into EtOH. The successful integration of Cs could also contribute to the observed improvements in dispersion and reduced agglomeration noted in the structural characterization, further supporting the catalyst's enhanced performance.

The XPS survey spectra presented in Fig. 6a provide a comprehensive overview of the elemental composition of the CuZnFe and *x*Cs/CuZnFe catalysts, where *x* represents different loadings of Cs. In the present study, XPS characterization was performed on calcined catalysts prior to the reduction step. This was done intentionally to examine the influence of Cs incorporation on the electronic environment of the Cu species and the surface composition in the oxidized state. The survey spectra indicate the presence of core-level peaks corresponding to C 1 s, O 1 s, Fe 2p, Cu 2p, Zn 2p, and Cs 3d in all samples. The presence of these peaks confirms that the CuZnFe catalysts have been successfully synthesized and that the Cs has been incorporated into the catalysts as intended. Fig. 6c presents the O 1 s spectra with two main peaks centered at 529.7 eV and 531.5 eV. The peak at 529.7 eV is typically assigned to lattice oxygen within the metal(s) oxide structure, while the peak at 531.5 eV corresponds to surface hydroxyl groups or adsorbed oxygen species. The Cs-modified catalysts show a slight shift and increased intensity in the higher binding energy component, suggesting an enhanced interaction between oxygen species and the catalyst surface, which may influence catalytic performance. Interestingly, a shoulder at 531.5 eV is observed only in the undoped CuZnFe and 4%Cs/CuZnFe samples. This shoulder is indicative of a higher concentration of surface hydroxyl groups or adsorbed oxygen species, which are critical for catalytic reactions involving oxygen. The presence of this shoulder in the 4%Cs/CuZnFe sample suggests that this particular Cs concentration optimizes the interaction between the catalyst surface and oxygen species, potentially enhancing catalytic activity. In contrast, the 2 %Cs/CuZnFe and 8%Cs/CuZnFe samples do not exhibit this shoulder, indicating a reduced presence of surface oxygen species. This absence might be due to insufficient surface modification at low Cs concentrations (2 %) or excessive surface passivation at high Cs concentrations (8 %), which can decrease the availability of active oxygen species necessary for catalytic processes.

The Cu 2p spectra, shown in Fig. 6d, feature two main peaks corresponding to Cu $2p_{3/2}$ and Cu $2p_{1/2}$ at binding energies of 933.8 eV and 953.6 eV, respectively. The presence of satellite peaks (at about 942 eV and 962 eV) suggests the coexistence of Cu^{2+} species [29,41]. For the 4%Cs/CuZnFe sample, the Cu $2p_{3/2}$ peak shifts slightly to a lower binding energy, from 933.8 eV to 933.0 eV. This shift indicates a change in the electronic environment of the Cu ions, likely resulting from an interaction between Cu and Cs atoms. The observed decrease in binding energy for the 4%Cs sample can be attributed to partial electron donation from Cs and/or alterations in the Cu coordination environment [27,42]. These phenomena are well-documented in literature for alkali-modified Cu-based catalysts and suggest a reduction of Cu^{2+} species to Cu^{1+}/Cu^0 or redistribution of charge density around Cu, which may influence its reducibility and catalytic behavior [37,43]. Interestingly, this binding energy shift correlates well with changes observed in the O 1 s spectra, suggesting that the Cs-induced modifications affect not only Cu but also the surface oxygen species. Together, these XPS results support our broader interpretation that the 4%Cs loading creates an optimized electronic environment, contributing to the enhanced

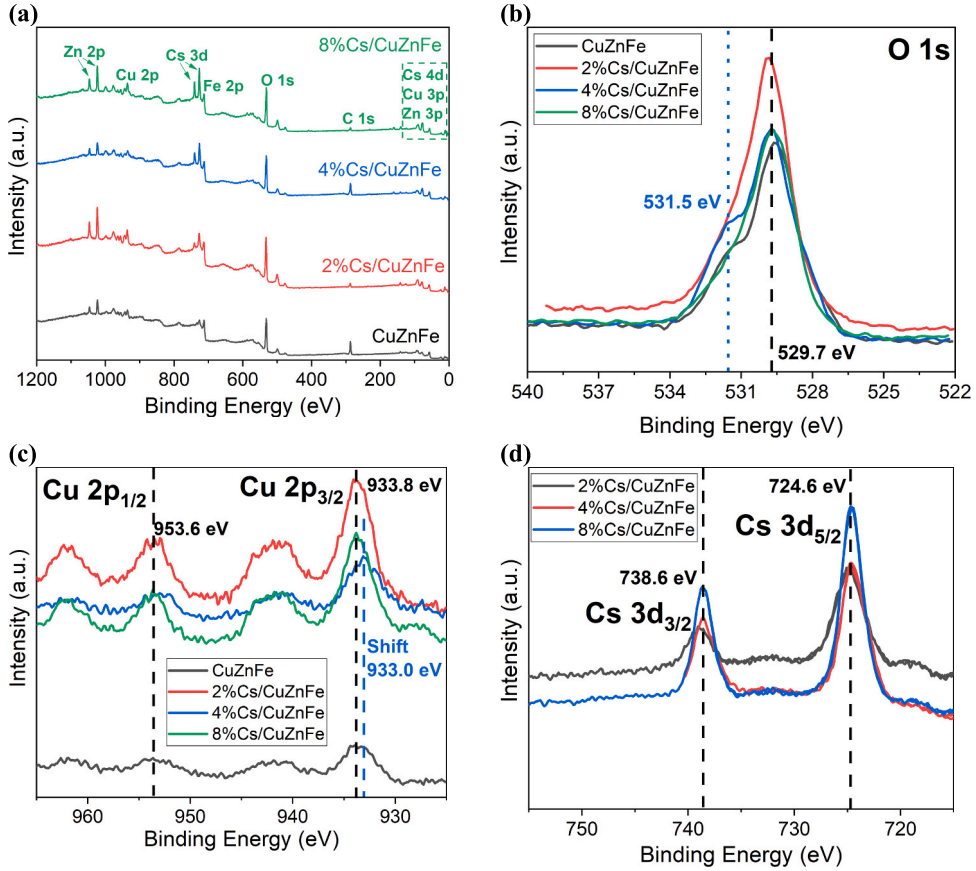

Fig. 6. XPS spectra of (a) – survey, (b) – O 1 s, (c) – Cu 2p, (d) – Cs 3d in the CuZnFe and *x*Cs/CuZnFe catalysts.

catalytic performance.

The Zn $2p_{3/2}$ spectra presented in Fig. S3b shows a prominent peak at 1021.4 eV, which is characteristic of Zn^{2+} species within the catalyst. This binding energy remains largely unchanged across all samples, indicating that the introduction of Cs does not have a significant effect on the electronic environment surrounding the Zn atoms in the catalyst. This stability in binding energy suggests that Zn maintains a consistent oxidation state, unaffected by Cs addition. However, the intensity of the Zn 2p3/2 peaks increases in the order: CuZnFe <4%Cs/CuZnFe <8%Cs/CuZnFe <2%Cs/CuZnFe. This trend implies that the presence and increasing concentration of Cs influences the overall composition or dispersion of Zn in the catalyst. The variation in peak intensity could also be attributed to changes in the catalyst morphology and/or surface area as more Cs is added, thereby increasing the detection of Zn in XPS measurements.

The Fe $2p_{3/2}$ spectra (Fig. S3c) display a peak at 710.3 eV, which corresponds to Fe^{3+} species. Similar to Zn, the binding energy of Fe remains largely unchanged upon Cs modification, indicating that the Fe species maintain their oxidation state and electronic environment within the catalyst matrix. Finally, the Cs 3d spectra in Fig. 6d show two peaks at 724.6 eV and 738.6 eV, corresponding to Cs $3d_{5/2}$ and Cs $3d_{3/2}$, respectively. These peaks confirm the successful incorporation of Cs into the catalyst structure. The intensity of these peaks increases with higher Cs loading, as expected, confirming the increasing amount of Cs on the catalyst surface. However, the 4%Cs/CuZnFe sample exhibits an intermediate Cs content, which we interpret as an optimal level of Cs coverage: sufficient to promote electron modification of Cu without excessively blocking active sites or inducing surface passivation, as may occur at higher loadings. Moreover, this Cu—Cs interaction correlates with the O 1 s spectra, which show enhanced intensity of the higher binding energy component (531.5 eV) in the 4%Cs sample, consistent with greater surface hydroxylation or adsorbed oxygen species.

The surface composition of the CuZnFe and *x*Cs/CuZnFe catalysts, as revealed by XPS analysis (Table S3), was determined. The unmodified CuZnFe catalyst shows a balanced surface composition but lacks the beneficial modification from Cs, potentially limiting its activity. The 4% Cs/CuZnFe catalyst has an intermediate oxygen content (46.8 %), compared to the 2 % (55.4 %) and 8 % (56.9 %) Cs/CuZnFe catalysts, suggesting that this oxygen level provides an optimal balance of lattice oxygen and surface hydroxyl groups necessary for redox reactions. The slightly lower Fe 2p content in the 4%Cs/CuZnFe catalyst (7.1 %) compared to the 2 %Cs/CuZnFe and 8%Cs/CuZnFe catalysts (9.0 % each) suggests a more finely dispersed or selectively exposed form of Fe, which could enhance catalytic activity. Despite having a lower Cu content (3.7 %) than the 2 %Cs/CuZnFe (10.1 %) and 8%Cs/CuZnFe (8.3 %) catalysts, the 4%Cs/CuZnFe catalyst's superior performance suggests that the quality or oxidation state of copper, rather than quantity, is crucial for catalytic efficiency. Additionally, the lower Zn 2p content (4.1 %) in the 4%Cs/CuZnFe catalyst, compared to the 2 %Cs/CuZnFe (10.5 %) and 8%Cs/CuZnFe (9.4 %) catalysts, indicates a more favorable distribution of Zn species, which can prevent agglomeration and maintain a high surface area for active sites. The intermediate Cs 3d content in the 4%Cs/CuZnFe catalyst (3.0 %) likely offers an optimal level of surface modification, enhancing basicity and electronic properties without excessively covering active sites, leading to its superior catalytic performance. The density of oxygen vacancies in these catalysts can also be estimated from the O 1 s spectra. As illustrated in Fig. 7, the O 1 s profiles reveal two distinct peaks upon deconvolution. The binding

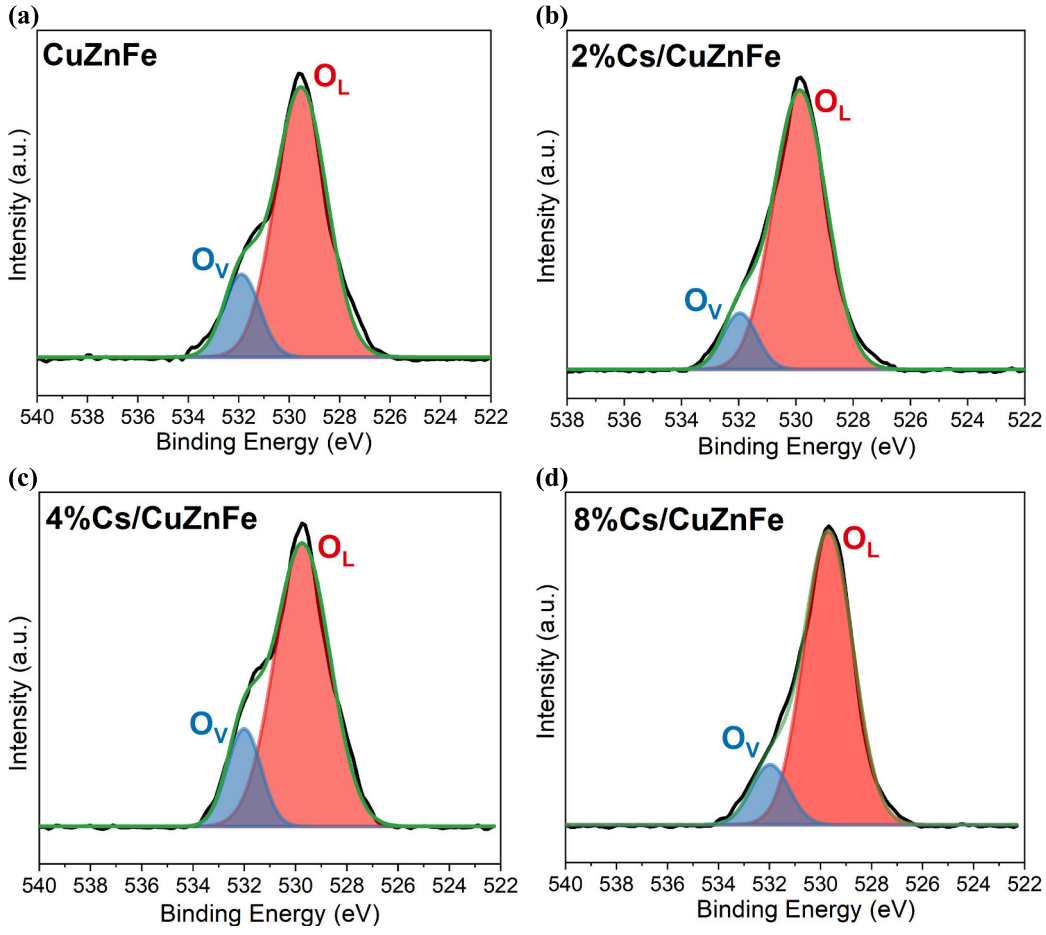

Fig. 7. Deconvoluted O 1 s XPS spectra of (a) – CuZnFe, (b) – 2 %Cs/CuZnFe, (c) – 4%Cs/CuZnFe, and (d) – 8%Cs/CuZnFe.

energy peaks observed at 529.5–529.8 eV and 531.8–532.0 eV correspond to lattice oxygen (O_L) and vacancy oxygen (O_V), respectively.

These findings align with previous studies [22,29,44], where O_L is typically attributed to oxygen atoms bound within the crystalline lattice of the oxide, representing oxygen in a stable, lattice-bound state. This O_L peak indicates the presence of well-ordered, stoichiometric oxide structures. On the other hand, the O_V peak is indicative of oxygen vacancies, which occur when oxygen atoms are absent from the lattice structure. These vacancies are critical as they often lead to changes in the material's electronic structure and catalytic activity. Oxygen vacancies play a significant role in enhancing surface reactivity, potentially creating active sites that facilitate catalytic processes. The presence of O_V suggests a more defective oxide structure, which can improve catalytic performance due to the higher density of active sites. As shown in Fig. S3d, the 4%Cs/CuZnFe catalyst exhibits the highest proportion of oxygen vacancies (17.5 %) compared to the 2 %Cs/CuZnFe (11.5 %) and 8%Cs/CuZnFe (13.7 %) catalysts, indicating that it contains the greatest number of oxygen vacancies. This finding implies that the presence of 4%Cs in the catalyst formulation may enhance the formation of oxygen vacancies, likely contributing to improved catalytic performance. The increased O_V concentration could be linked to enhanced redox properties or oxygen mobility, which is often beneficial for reactions such as CO_2 hydrogenation processes. Taken together, the Cu 2p binding energy shift, the optimized Cs 3d content, and the increased oxygen vacancy concentration support the conclusion that at 4%Cs, there is a strong and favorable synergistic interaction between Cs and Cu. This interaction modifies the electronic environment of Cu, likely making it more reducible and catalytically active.

The adsorption and activation of CO_2 over the CuZnFe and *x*Cs/CuZnFe catalysts are crucial for facilitating CO_2 conversion into reaction intermediates and subsequent C—C coupling processes, which directly impact catalytic performance. To evaluate the CO_2 adsorption capacity and basic site distribution, CO_2-TPD measurements were conducted, as shown in Fig. 8. The desorption profiles (Fig. 8a) reveal three distinct temperature regions corresponding to different types of CO_2 adsorption sites: the low-temperature region (50–300 °C) associated with CO_2 adsorbed on hydroxyl groups, the medium-temperature region (300–570 °C) attributed to surface medium-strength basic sites or oxygen vacancies, and the high-temperature region (above 570 °C) assigned to coordination-unsaturated O^{2-} species, which exhibit strong basicity [45]. The CO_2-TPD results indicate significant variations in CO_2 adsorption capacities among the studied catalysts. The unmodified CuZnFe catalyst exhibits moderate total basicity, with a balanced contribution from weak, moderate, and strong basic sites.

The introduction of 2 %Cs enhances moderate basic sites, as evidenced by the increased desorption intensity around 434.6 °C, suggesting that Cs incorporation modifies the electronic environment, promoting stronger interactions with CO_2. However, the 4%Cs/CuZnFe catalyst exhibits the lowest CO_2 adsorption capacity and total basicity compared to both the unmodified CuZnFe and the other Cs-promoted catalysts. This phenomenon can be attributed to an increased Cu surface concentration, as confirmed by ICP-OES and SEM-EDX analysis, which suggests that the surface Cs species are covered by Cu, thereby reducing the accessibility of basic sites for CO_2 adsorption. Interestingly, despite its lower total basicity, the 4%Cs/CuZnFe catalyst exhibits the highest catalytic activity in CO_2 hydrogenation to ethanol among all studied samples. These results indicate that a high CO_2 adsorption capacity does not necessarily correlate with improved catalytic performance. In the case of the 4%Cs/CuZnFe catalyst, the combination of moderate basic site density and a high concentration of oxygen vacancies may offer a more favorable environment for CO_2 activation. This environment likely promotes efficient formation of reactive intermediates while avoiding excessive CO_2 adsorption, which could otherwise hinder C—C coupling or lead to unwanted side reactions. The electronic and structural modifications induced by the 4%Cs loading likely enhance the synergy between Cu and ZnFe components, promoting C—C coupling and ethanol selectivity. In contrast, the 8%Cs/CuZnFe catalyst exhibits the highest total CO_2 desorption, with a dominant contribution from strong basic sites at high temperatures (above 570 °C). While these strong basic sites enhance CO_2 activation, their excessive presence may lead to over-adsorption of CO_2, resulting in reduced catalytic efficiency due to the formation of unwanted byproducts. This explains why the 8%Cs/CuZnFe catalyst, despite its high CO_2 adsorption capacity, does not outperform the 4%Cs/CuZnFe sample in ethanol production. The CO_2 desorption capacities (Fig. 8b) further support these observations. The 2 %Cs/CuZnFe catalyst maintains a well-balanced distribution of weak, moderate, and strong basic sites, which contribute to its relatively good CO_2 adsorption and catalytic performance. The 4%Cs/CuZnFe catalyst, despite showing the lowest total CO_2 desorption, demonstrates the highest ethanol yield, reinforcing the idea that optimal catalytic activity is achieved through a synergy between electronic and structural modifications induced by Cs, optimal Cu dispersion, oxygen vacancy formation, and a moderate level of basicity. These combined effects contribute to its superior catalytic behavior, even though its CO_2 adsorption capacity appears lower in quantitative terms. The 8%Cs/CuZnFe catalyst, on the other hand, shows an increase in total basicity, dominated by strong sites, which may enhance CO_2 adsorption but not necessarily improve ethanol selectivity. These findings suggest that efficient ethanol synthesis may be favored not by maximizing CO_2 adsorption capacity, but rather by achieving a synergistic balance between oxygen vacancy-induced activation and moderate CO_2 binding strength, which together promote C—C coupling and selective ethanol formation.

The in situ DRIFTS analysis of the CO_2 hydrogenation reaction over the 4%Cs/CuZnFe catalyst provided valuable insights into the surface species and reaction mechanisms involved in ethanol and HA formation

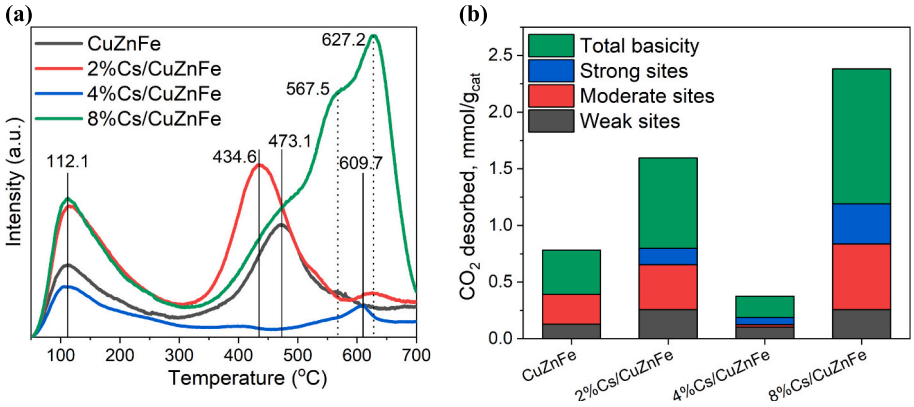

Fig. 8. The CO_2-TPD – (a) and CO_2 desorption results – (b) for the CuZnFe and *x*Cs/CuZnFe catalysts.

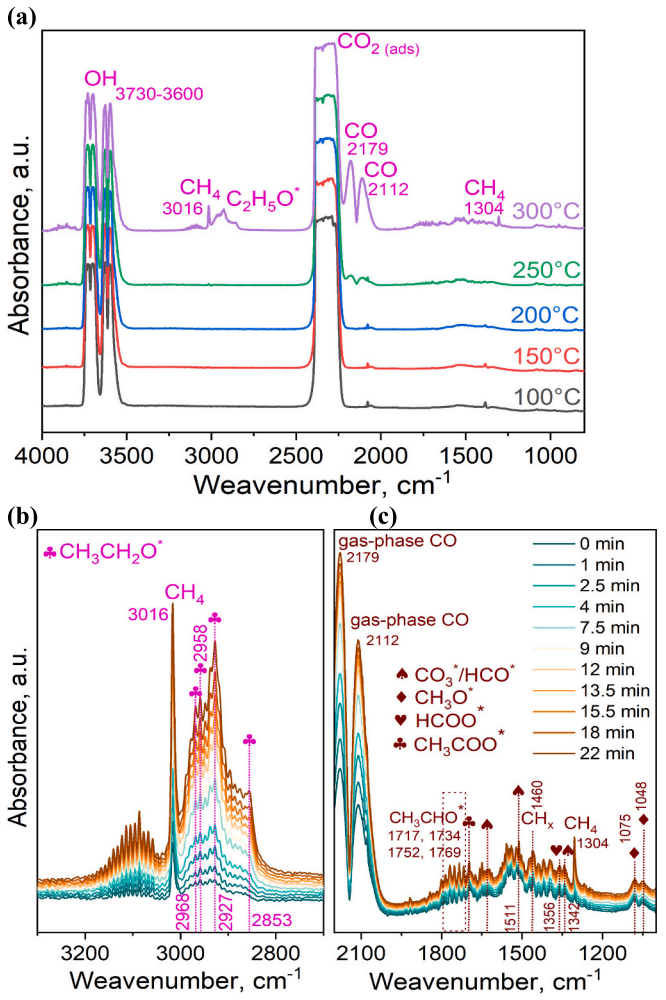

Fig. 9. In situ DRIFT spectra of surface species on the 4%Cs/CuZnFe catalyst during CO_2 hydrogenation (H_2/CO_2 = 3/1, P = 20 bar): (a) – spectra at different temperatures; (b, c) – time-resolved spectra at 300 °C.

(Fig. 9 and Fig. S6). Upon exposure to the CO_2/H_2 mixture, the formation of gaseous CO was detected (Fig. 9a), with a significant increase observed between 250 and 300 °C, as evidenced by the appearance of characteristic bands at 2112 cm^{-1} and 2179 cm^{-1} [46,47]. These spectral features indicated that the RWGS reaction occurred rapidly, converting CO_2 to CO, which subsequently participated in further transformation pathways. The CO_2 adsorption process was characterized by absorption bands in the 2220–2500 cm^{-1} region, confirming rapid surface interaction [48]. The bands in the 3730–3600 cm^{-1} region attributed to surface hydroxyl groups, including terminal –OH and hydrogen-bonded OH species [49,50]. These features suggest the presence of adsorbed water or reaction intermediates, highlighting the active role of surface hydroxyls in the CO_2 hydrogenation process. The appearance of bands at 3016 and 1306 cm^{-1} indicates the formation of CH_4 as a side product at high temperature (300 °C), with increasing intensity over time, suggesting progressive methane formation during the reaction [51–53]. This suggests a tendency for adsorbed CO species to undergo dissociation and subsequent hydrogenation [54]. The appearance of *CO_3^*, HCO^*, and $HCOO^*$ species* around 1300–1600 cm^{-1} suggests that Cs modification enhances CO_2 activation, leading to the formation of surface-bound intermediates crucial for ethanol synthesis [48,55].

The spectral region 2900–3000 cm^{-1} in Fig. 9b exhibits key vibrations associated with C—H stretching modes of surface ethoxide ($C_2H_5O^*$) species. The peaks at 2968, 2958, 2927, and 2853 cm^{-1} correspond to the asymmetric and symmetric stretching of -CH_3 and -CH_2 groups, signifying the formation of C_2 intermediates [46]. Notably, these bands intensify with increasing time and temperature, indicating the progressive accumulation of ethoxide species, which are key intermediates in ethanol formation via a CO insertion mechanism.

Fig. 9c further confirms the evolution of intermediates. The bands at 1717, 1734, 1752, and 1769 cm^{-1} are characteristic of acetaldehyde (CH_3CHO) species, supporting the hypothesis that ethanol formation proceeds through an intermediate CO → CH_3CHO → C_2H_5OH pathway [56]. The appearance of HCOO* (1356 cm^{-1}), CH_3O^* (1460 cm^{-1}), and CH_3COO^* (1342 cm^{-1}) vibrations suggests that formate, methoxy, and acetate species are crucial reaction intermediates, with their intensities increasing at longer reaction times and high temperatures. The carbonate-related bands at 1511 cm^{-1} and 1628 cm^{-1} further highlight the interaction between CO_2 and the catalyst surface, indicating that the moderate alkalinity induced by Cs doping enhances the stabilization of formate and carbonate species, facilitating C—C coupling. Further analysis of the DRIFT spectra indicated a strong interaction between Cs and reaction intermediates. The presence of a peak at 1356 cm^{-1}, assigned to HCOO* species associated with Cs^+, suggested that Cs played a crucial role in stabilizing these intermediates [57].

Moreover, the 4%Cs/CuZnFe catalyst exhibited enhanced adsorption of carbonate (CO_3*) and HCO* species, as reflected in the bands at 1511, 1628, and 1342 cm^{-1} [58]. This finding indicated that Cs introduction increased the surface alkalinity, which favored the adsorption of key reaction intermediates and promoted C—C coupling. The observed spectral features aligned well with the proposed reaction mechanism below, where CO formed on the catalyst surface initially reacted with iron to generate Fe_5C_2 or chemisorbed CO species. These species subsequently underwent hydrogenation to form HCOO*, which acted as a precursor for ethanol synthesis via C—C bond formation. The ability of the 4%Cs/CuZnFe catalyst to enhance CO_2 activation and stabilize key intermediates highlights its efficacy in promoting selective ethanol production. The in situ DRIFTS analysis demonstrates that ethanol formation occurs via a multi-step pathway involving CO_2 activation, CO formation (RWGS), formate/methoxy intermediates, CO insertion, and ethoxide-mediated ($C_2H_5O^*$) chain growth. The presence of Cs in the CuZnFe catalyst plays a critical role in enhancing CO_2 adsorption, stabilizing key intermediates, and promoting the formation of short-chain oxygenates like ethanol. These findings align well with the reaction performance, confirming that moderate Cs loading is beneficial for selective ethanol synthesis from CO_2 hydrogenation.

3.2. Catalytic performance

3.2.1. The effect of Cs loading, reaction time and temperature on the composition of the gas products

Fig. 10 presents a comprehensive analysis of the performance of CuZnFe and *x*Cs/CuZnFe catalysts in the gas phase for CO_2 hydrogenation, with a focus on CO_2 conversion, STY, selectivity of C_{2+} alcohols or EtOH, and MeOH selectivity. Fig. 10a illustrates the CO_2 conversion over TOS for the different catalysts at three distinct temperatures: 200, 250, and 300 °C. Initially, at 200 °C, all catalysts exhibit relatively low CO_2 conversion rates, with minimal differences among them.

However, as the temperature increases to 250 °C and subsequently to 300 °C, a significant enhancement in CO_2 conversion is observed across all catalysts. Notably, the Cs-promoted catalysts, particularly the 4%Cs/CuZnFe and 8%Cs/CuZnFe, demonstrate superior performance compared to the unmodified CuZnFe catalyst. The highest CO_2 conversion is achieved at 300 °C, indicating that elevated temperatures favour the activation and conversion of CO_2 over these catalysts. In Fig. 10b, the STY of C_{2+} alcohols and/or EtOH is depicted as a function of TOS for the catalysts at the same temperature ranges. At 200 °C, the STY values are minimal, aligning with the low CO_2 conversion observed. As the temperature rises to 250 °C, an increase in STY is noted, with the Cs-promoted catalysts again outperforming the unmodified CuZnFe

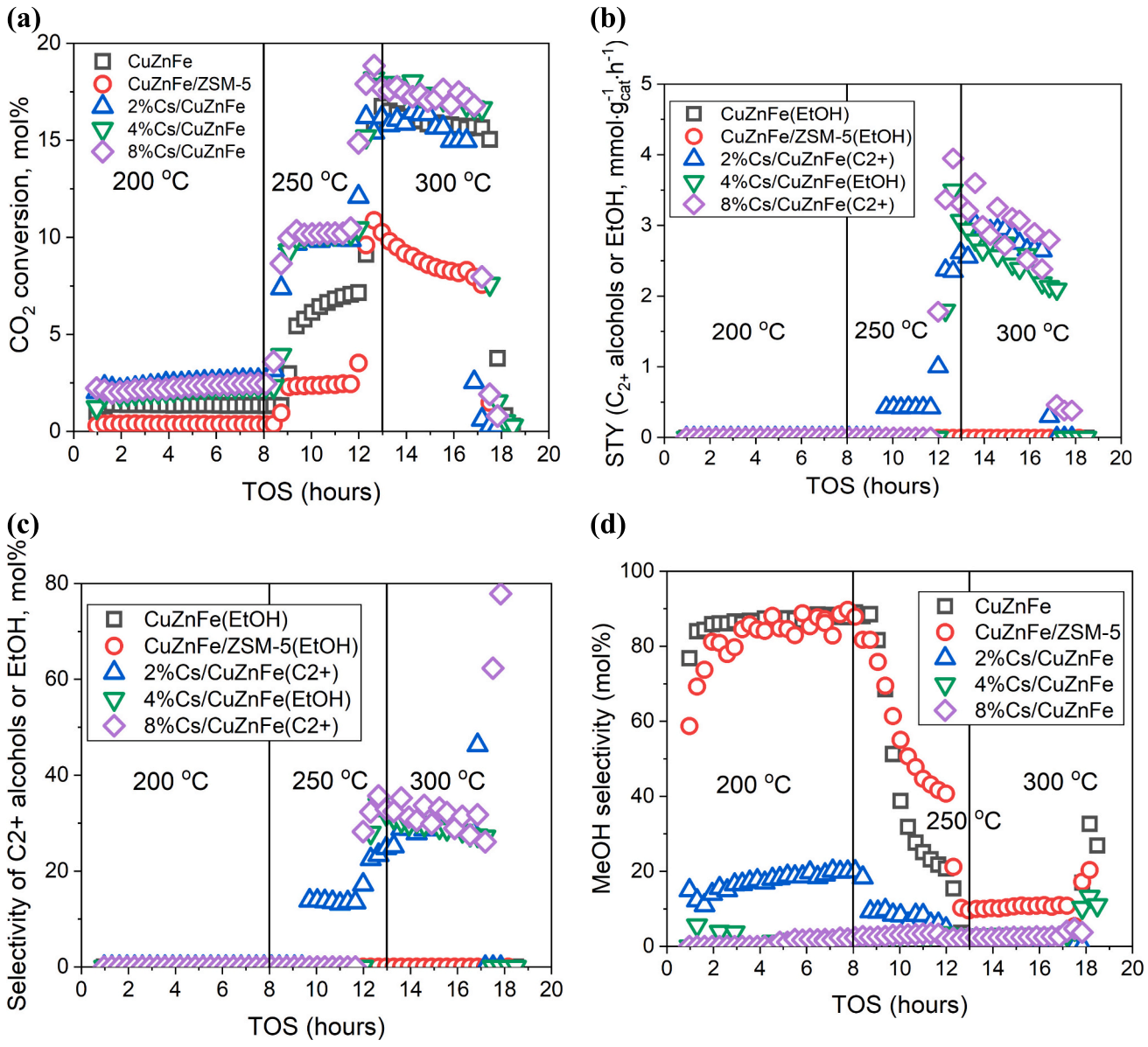

Fig. 10. CO_2 conversion – (a), STY – (b), selectivity of C_{2+} alcohols or EtOH – (c) and MeOH selectivity – (d) over the CuZnFe and *x*Cs/CuZnFe catalysts in the gas phase. Reaction conditions: $m_{catalyst}$ = 250 mg; H_2/CO_2 = 3; P = 20 bar; GHSV = 9917 h^{-1}; TOS = 19 h; T = 200–300 °C.

catalyst. The trend continues at 300 °C, where the STY reaches its peak for the 4%Cs/CuZnFe and 8%Cs/CuZnFe catalysts, suggesting that Cs promotion significantly enhances the catalytic activity for the formation of HA and EtOH. Fig. 10c shows the selectivity of C_{2+} alcohols or EtOH in mol% over the different catalysts. At 200 °C, the selectivity remains low across all catalysts. As the temperature increases to 250 °C and further to 300 °C, there is a noticeable rise in the selectivity of C_{2+} alcohols and/or EtOH, particularly for the Cs-modified catalysts. The 8% Cs/CuZnFe catalyst exhibits the highest selectivity at 300 °C, indicating that higher Cs loading promotes the formation of C_{2+} alcohols and EtOH over MeOH.

Fig. 10d illustrates the MeOH selectivity over TOS for the studied catalysts. At 200 °C, the CuZnFe/ZSM-5 catalyst shows the highest MeOH selectivity, maintaining a stable performance over the entire TOS. As the temperature increases to 250 °C and then to 300 °C, the MeOH selectivity decreases for all catalysts, with a more pronounced decline for the Cs-promoted catalysts. This inverse relationship between methanol selectivity and temperature suggests that higher temperatures and Cs promotion favour the production of HA and EtOH over MeOH.

3.2.2. The effect of Cs loading on the composition of the liquid products and STY

Fig. 11 illustrates the effect of Cs loading on the STY and product selectivity over CuZnFe and Cs-loaded CuZnFe catalysts in the liquid phase. As shown in Fig. 11a, the introduction of Cs to the CuZnFe catalyst significantly impacts the production rates of MeOH and EtOH. The CuZnFe catalyst without Cs shows minimal STY for both MeOH and EtOH. With 2 %Cs loading, the STY of EtOH increases noticeably, reaching approximately 1.0 $mmol \cdot g_{cat}^{-1} \cdot h^{-1}$, while the STY of methanol remains low. At 4%Cs loading, ethanol STY peaks and maintains the highest value observed (~1.2 $mmol \cdot g_{cat}^{-1} \cdot h^{-1}$), whereas methanol STY stays relatively low and constant. However, at 8%Cs loading, the STY of EtOH drops significantly, indicating that excessive Cs may inhibit ethanol production, while methanol STY remains largely unchanged. Fig. 11b provides detailed insights into product selectivity over various catalysts, complementing the STY trends observed in Fig. 11a and highlighting the distribution of various liquid-phase products, including alcohols, acids, and other compounds. For the CuZnFe catalyst, methanol is the main product, with a selectivity of approximately 70 %,

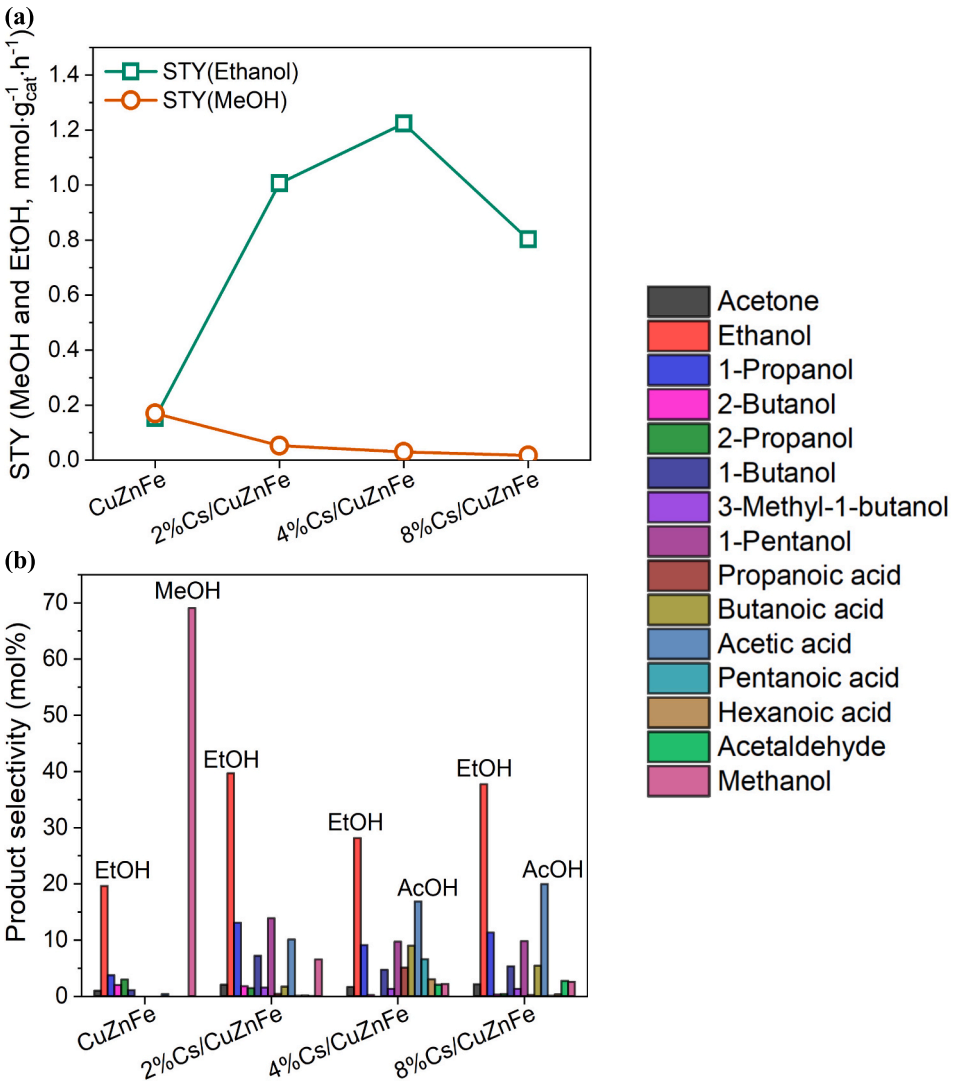

Fig. 11. (a) – STY and (b) – product selectivity over the CuZnFe and *x*Cs/CuZnFe catalysts in the liquid phase. Reaction conditions: $m_{catalyst}$ = 250 mg; H_2/CO_2 = 3; *P* = 20 bar; GHSV = 9917 h^{-1}; TOS = 19 h; *T* = 200–300 °C.

alongside minor quantities of ethanol, acetone, 1-propanol, 2-butanol, 2-propanol, and 1-butanol. With the addition of 2 %Cs to CuZnFe, ethanol selectivity surges to around 40 %, while MeOH selectivity decreases to about 10 %.

Additionally, minor products such as 1-propanol, 1-pentanol, and acetic acid are present in low quantities. At 4%Cs/CuZnFe, ethanol selectivity remains around 30 %, indicating that this Cs loading favors ethanol production, but at the same time, more byproducts are formed and detected in the reaction mixture. In contrast, methanol selectivity drops significantly compared to the CuZnFe catalyst, with moderate amounts of acetic acid and other byproducts. At 8%Cs/CuZnFe, selectivity shifts notably toward acetic acid (~20 %), with ethanol selectivity increasing to around 40 %, and methanol remaining a minor product. These results suggest that Cs loading alters the catalytic pathways, promoting different products at varying Cs concentrations. Moderate Cs loading (4 %) optimizes ethanol production, but shifts the selectivity toward acetic acid and other byproducts, possibly due to changes in the active sites or reaction intermediates.

3.2.3. The product distribution over 4%Cs/CuZnFe catalyst at different reaction temperatures in the gas phase

The performance of the 4%Cs/CuZnFe catalyst in the gas-phase conversion of CO_2 to various products was evaluated under varying temperature conditions (200–300 °C) as illustrated in Fig. 12a. The product selectivity profile shows distinct trends for different hydrocarbons and oxygenates as the temperature increases from 200 to 300 °C. At 200 °C, CH_4 is the predominant product, with its selectivity starting at approximately 90 % and decreasing gradually to about 70 % over 8 h. C_2H_4 and C_2H_6 exhibit a slight increase in selectivity, stabilizing around 10–15 % after 8 h. EtOH and MeOH show minimal selectivity at this temperature. At 250 °C, the selectivity for CH_4 continues to decline, settling around 60 %. The selectivity for EtOH increases significantly, reaching approximately 30 % after 12 h. C_2H_4 and MeOH exhibit a minor increase in selectivity, with C_2H_6 stabilizing around 10 %. When the temperature is further increased to 300 °C, CH_4 selectivity drops sharply to about 40 %. Conversely, the selectivity for EtOH peaks at this temperature, keeps stable achieving nearly 30 %. The selectivity for C_2H_4 decreases slightly but remains significant at around 20 %. MeOH and C_2H_6 selectivity remains low and stable, with slight increase to 10 % after 17 h.

Fig. 12b shows the STY of various products at different temperatures. At 200 °C, the STY values for all detected products were low, with CH_4 having the highest STY of <0.3 mmol·g_{cat}^{-1}·h^{-1}. When the temperature increased to 250 °C, the STY of CH_4 rose to 1.6 mmol·g_{cat}^{-1}·h^{-1}, while the STY of other products remained nearly unchanged. A significant change was observed at 300 °C, where the STY of EtOH increased markedly to

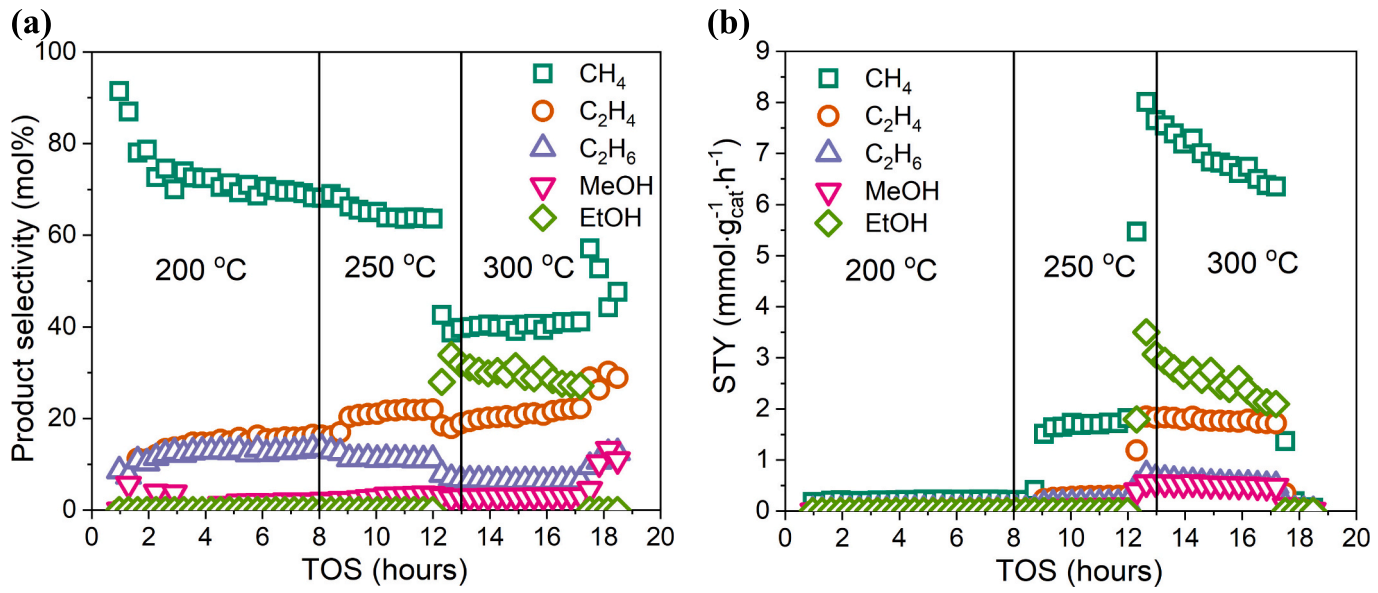

Fig. 12. (a) – product distribution and (b) – STY over the 4%Cs/CuZnFe catalyst in the gas phase. Reaction conditions: $m_{catalyst}$ = 250 mg; H_2/CO_2 = 3; P = 20 bar; GHSV = 9917 h^{-1}; TOS = 19 h; T = 200–300 °C.

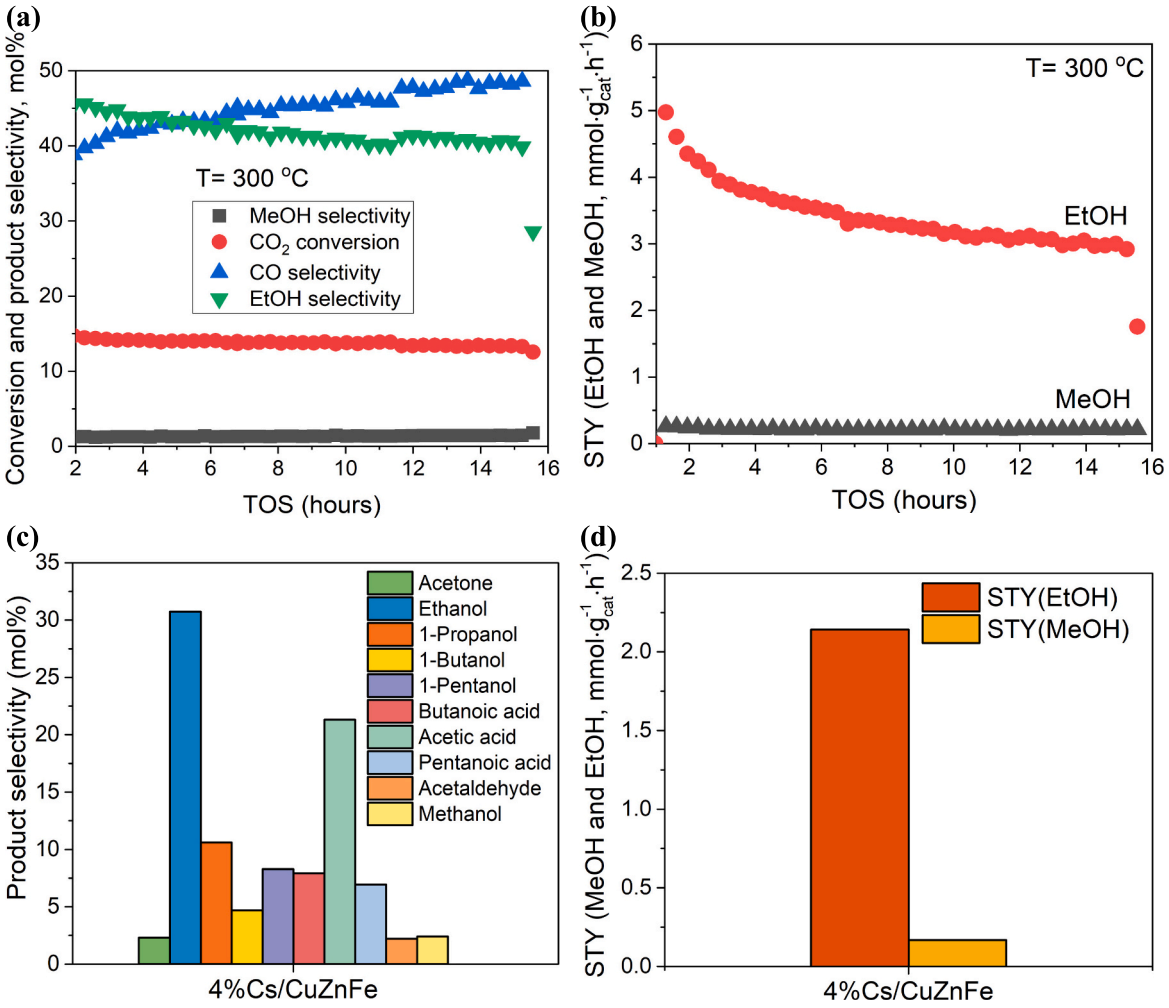

Fig. 13. (a, b) – product selectivity and STY over the 4%Cs/CuZnFe catalyst in the gas phase; (c, d) – product selectivity and STY over the 4%Cs/CuZnFe catalyst in the liquid phase. Reaction conditions: $m_{catalyst}$ = 250 mg; H_2/CO_2 = 3; P = 20 bar; GHSV = 9917 h^{-1}; TOS = 16 h; T = 300 °C.

3.5 mmol·g_{cat}^{-1}·h^{-1}. During this time, the STY of CH_4 initially increased to 8.0 mmol·g_{cat}^{-1}·h^{-1} but subsequently decreased to 1.4 mmol·g_{cat}^{-1}·h^{-1} after 17 h. Additionally, the STY for C_2H_4, C_2H_6, and MeOH increased, with C_2H_4 reaching around 1.8 mmol·g_{cat}^{-1}·h^{-1}, and C_2H_6 and MeOH reaching approximately 0.5–0.7 mmol·g_{cat}^{-1}·h^{-1} each. The data indicate that the 4%Cs/CuZnFe catalyst exhibits a strong temperature dependence in its activity and selectivity for CO_2 hydrogenation. At lower temperatures (200–250 °C), CH_4 is the main product. As the temperature increases, there is a noticeable shift toward higher selectivity and STY for ethanol and ethylene, especially at 300 °C. This suggests that higher temperatures favour the formation of more valuable C_{2+} oxygenates and hydrocarbons, potentially due to enhanced activation and hydrogenation of CO_2 and intermediates. The ability to tune the product distribution by adjusting the reaction temperature highlights the versatility of the 4% Cs/CuZnFe catalyst in CO_2 hydrogenation applications.

Fig. 13a and Fig. 13b illustrate the performance of the 4%Cs/CuZnFe catalyst in the gas phase. In Fig. 13a, the CO_2 conversion remains relatively stable around 15 % throughout the 16 h period, indicating relatively good stability of the catalyst. The CO selectivity increases slightly over time, reaching around 50 % at the end of the experiment. Further details on the effect of reaction temperature and time on CO selectivity are provided in Fig. S4. EtOH selectivity decreases slightly after an initial peak, stabilizing around 40 %. MeOH selectivity, on the other hand, is relatively low but stable, hovering around 2 %. Fig. 13b focuses on the STY of EtOH and MeOH. The STY of EtOH starts high at approximately 5.0 mmol·g_{cat}^{-1}·h^{-1} but gradually decreases to about 3.0 mmol·g_{cat}^{-1}·h^{-1} by the end of the 16 h period. The STY of MeOH remains consistently low, around 0.2 mmol·g_{cat}^{-1}·h^{-1}, reflecting its lower selectivity.

Fig. 13c-d and Fig. S5 present the product selectivity and STY of the 4%Cs/CuZnFe catalyst in the liquid phase under identical reaction conditions. Fig. 13c illustrates a diverse range of products, with EtOH being the most selective, accounting for over 30 % of the total product composition. Other alcohols, such as 1-propanol, 1-butanol, 1-pentanol, and methanol, each range between 2 and 10 %. Additionally, acetic acid demonstrates significant selectivity at approximately 20 %, while other detected acids, including butanoic and pentanoic acid, range between 7 and 8 %. The presence of various alcohols and acids indicates a complex reaction network, likely involving multiple reaction pathways.

The data presented in Fig. 13d demonstrates a significant disparity in the STY between EtOH and MeOH. Specifically, the STY for EtOH is substantially higher than that for MeOH, with ethanol achieving an STY of approximately 2.2 mmol·g_{cat}^{-1}·h^{-1}, whereas MeOH only reaches around 0.1 mmol·g_{cat}^{-1}·h^{-1}. This observation is consistent with the selectivity data, indicating a preferential formation of EtOH over MeOH by the catalyst. Furthermore, the STY of EtOH varies notably between the gas and liquid phases. In the gas phase, ethanol achieves an impressive STY of 5.0 mmol·g_{cat}^{-1}·h^{-1}, which is significantly higher than its STY in the liquid phase. On the other hand, the STY of MeOH remains consistently low across both phases. This further underscores the catalyst preferential activity toward EtOH production under the given experimental conditions. These findings suggest that the catalytic conditions and the nature of the catalyst employed are highly favorable for EtOH production. The stark contrast in STY between EtOH and MeOH

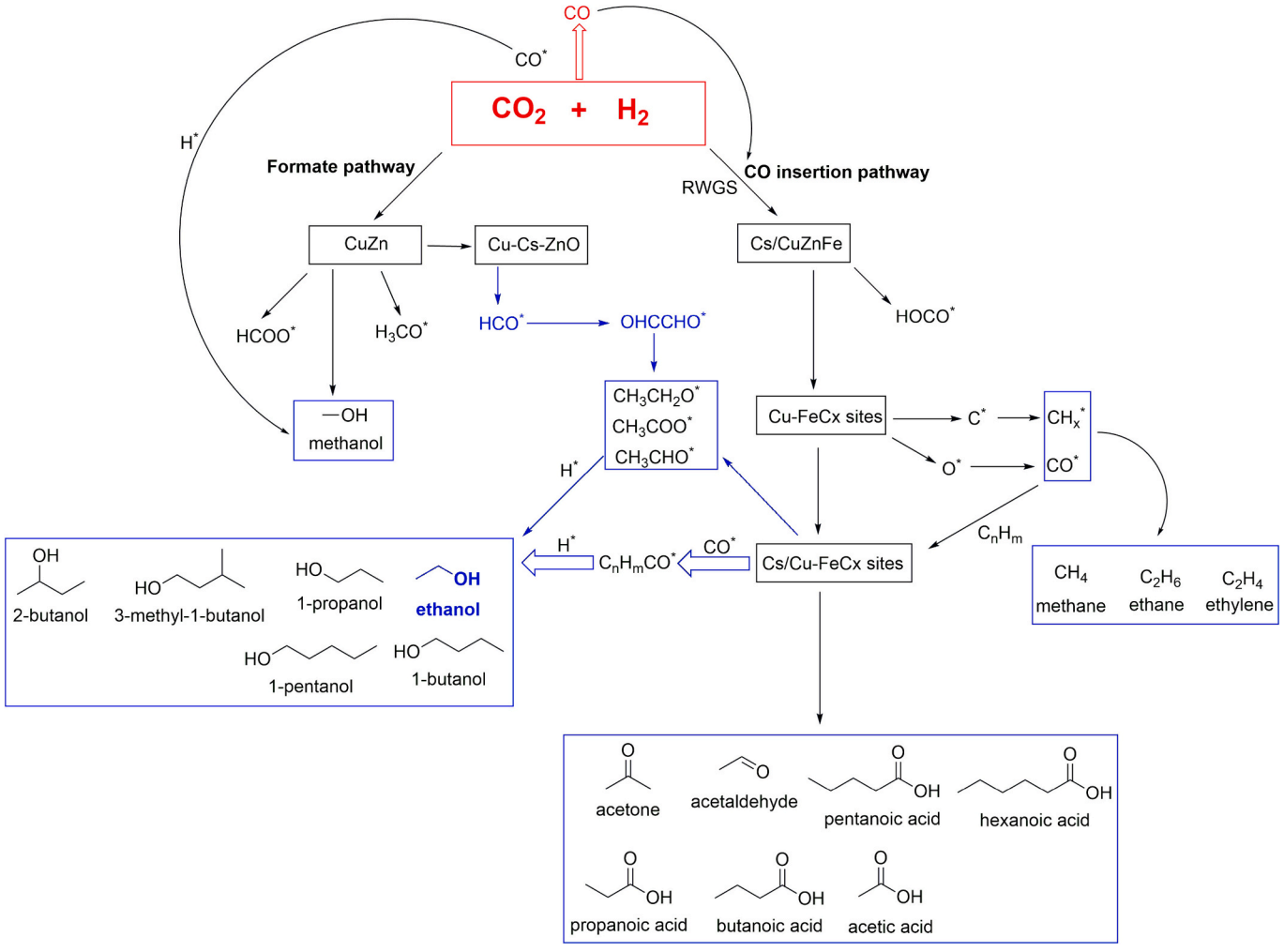

Fig. 14. The reaction pathways of CO_2 hydrogenation over the *x*Cs/CuZnFe catalysts.

indicates that the reaction conditions are optimized for EtOH formation.

3.3. Reaction mechanism

The reaction pathways of CO_2 hydrogenation over the *x*Cs/CuZnFe catalysts, illustrated in Fig. 14, can be classified into two primary mechanisms: the formate pathway and the CO insertion pathway, which are consistent with the in situ DRIFTS observations presented in Fig. 9 and Fig. S6. These pathways are intricately governed by the catalyst composition, electronic interactions, and active site modifications, particularly the effect of Cs as a promoter. In the formate pathway, CO_2 and H_2 initially react to form surface-bound formate intermediates (*HCOO and *H_3CO), facilitated by the CuZn interfaces. These formate species serve as key intermediates in the stepwise reduction to methanol [28]. The presence of the Cs promoter, however, alters the reaction dynamics, impeding methanol formation by redirecting intermediates toward HA and hydrocarbons. Electronic structure analysis suggests that Cs ions influence the electronic properties of the CuZnFe interface, thereby modulating the adsorption energies and stabilization of key oxygenated intermediates. Sun et al. [59] demonstrated through Bader charge analysis that Cs ions enhance nucleophilic coupling between HCO (HCO + HCO) and H_2CO (H_2CO + HCO) species, thereby promoting initial C − C bond formation. This behavior aligns with the observations of Wang et al. [30], who reported that the Cs-promoting effect on C − C coupling is driven by a synergistic interaction among Cs, Cu, and ZnO. At the Cu − Cs − ZnO interface, the unique electronic configuration stabilizes CH_x and CH_yO species, facilitating the chain propagation necessary for HA synthesis. Further insights from density functional theory (DFT) and kinetic Monte Carlo (KMC) simulations have shed light on the fundamental role of Cs in stabilizing O-anchored intermediates such as *CO_2, *HCOOH, *CHO, and *CH_2O [30]. The stabilization is primarily attributed to the formation of strong O − Cs bonds at the Cu − Cs − ZnO interface, which enhances the adsorption strength and lifetime of intermediates. This, in turn, influences reaction selectivity by shifting equilibrium pathways away from methanol and toward multi-carbon oxygenates. Moreover, experimental studies indicate that the presence of Cs modulates the activation barrier for the hydrogenation of *CHO and *CH_2O, thereby facilitating the formation of ethanol and other higher oxygenates. The redistribution of electron density across the Cs-modified CuZn interface contributes to enhanced CO_2 conversion rates and improved selectivity toward ethanol and HA.

The CO insertion mechanism is widely recognized as the dominant pathway for C_{2+} oxygenate formation during CO_2 hydrogenation, particularly in a fixed-bed reactor [57]. The reaction sequence begins with the reverse water-gas shift (RWGS) reaction, where CO_2 is converted into CO and H_2O. The CO subsequently participates in formyl radical (HOCO*) formation over the Cs/CuZnFe catalyst, a key step that dictates the overall pathway toward HA and hydrocarbons. Upon formation, HOCO* undergoes decomposition into surface-bound C* and O* species at Cu − FeC_x sites. The resulting carbon radicals can follow multiple reaction routes: hydrogenation leads to the formation of methane, ethane, and ethylene, oxygen radicals interact with carbon radicals, regenerating CO* species, and HA such as ethanol, 1-propanol, 2-butanol, 1-pentanol, and 3-methyl-1-butanol arise from the sequential hydrogenation of corresponding aldehydes and ketones at Cs/Cu − FeC_x sites. Further oxidation and hydrogenation steps involving CO intermediates contribute to the formation of carboxylic acids, including acetic acid, propanoic acid, butanoic acid, pentanoic acid, and hexanoic acid.

The CO insertion mechanism is particularly significant due to its ability to generate a diverse range of oxygenated products beyond methanol. According to the literature [30], DFT studies highlight that Cs plays a crucial role in stabilizing CO insertion intermediates by altering the electronic landscape of Cu − FeC_x active sites. This modification reduces activation barriers for C − C bond formation and shifts product selectivity toward longer-chain oxygenates. The mechanistic understanding of CO_2 hydrogenation over *x*Cs/CuZnFe catalysts underscores several key strategies for catalyst optimization. Electronic modulation through fine-tuning the electronic properties of CuZnFe interfaces via Cs promoters enhances selectivity toward ethanol and HA. Surface stability is improved through the stabilization of O-anchored intermediates via strong O − Cs bonds, which extends catalyst lifetime and minimizes deactivation. Additionally, kinetic control plays a crucial role in balancing CO and H_2 activation pathways, preventing excessive side reactions and optimizing product distribution. Overall, the CO_2 hydrogenation mechanism over *x*Cs/CuZnFe catalysts involves intricate interactions between the formate and CO insertion pathways. The presence of Cs significantly influences the reaction network by stabilizing key intermediates, modulating electronic properties, and enhancing C − C coupling. Furthermore, the synergistic role of Cs promoters in optimizing CO activation and hydrogenation kinetics plays a pivotal role in steering product selectivity toward ethanol and HA. Future research directions should focus on refining catalyst composition and reactor conditions to further enhance process efficiency and scalability for industrial applications.

In our catalytic system, Cs does not simply act as a promoter of surface basicity. Rather, it induces substantial structural and electronic modifications to the CuZnFe catalyst, as confirmed by multiple characterization techniques. XRD patterns reveal the presence of crystalline $CsNO_3$ domains, indicating the formation of new phases not observed in earlier studies. SEM and BET analyses show significant morphological changes, including a more open and porous surface with reduced particle aggregation. SEM-EDX and ICP-OES demonstrate redistribution of surface elements, while XPS reveals a shift in the Cu $2p_{3/2}$ binding energy, suggesting a modified electronic environment due to Cs—Cu interactions and a possible change in Cu oxidation state.

These changes impact both surface basicity and CO_2 adsorption behavior. Notably, the 4%Cs/CuZnFe catalyst exhibits the lowest total CO_2 uptake, yet delivers the highest ethanol selectivity and the highest space-time yield of C_{2+} alcohols (5.0 mmol·g_{cat}^{-1}·h^{-1}). This indicates that CO_2 adsorption capacity alone does not dictate catalytic performance. Instead, the optimal performance arises from a well-balanced synergy among Cu, Zn, Fe, and Cs, which enhances CO_2 activation, promotes selective C—C coupling, and suppresses side reactions, likely due to a more favorable electronic and structural environment. In summary, the role of Cs in our system is multifunctional: it not only enhances the basicity of the catalyst but also alters its morphology, metal dispersion, and electronic properties, resulting in a distinct catalytic behavior. These effects clearly differentiate our system from previous reports and contribute a novel perspective to the design of alkali-promoted Cu-based catalysts for CO_2 hydrogenation.

4. Conclusions

In summary, our study focuses on a catalyst composed of Cs, Cu, Zn, and Fe, which has shown promising results in synthesizing C_{2+} alcohols with a high selectivity (78.8 mol%) and a CO_2 conversion rate of 17.0 %. Notably, the 4%Cs/25%Cu − 25%Zn − 50%Fe catalyst demonstrates a remarkable STY for ethanol of 5.0 mmol·g_{cat}^{-1}·h^{-1} in the gas phase, representing a substantial advancement over catalysts reported in the literature. This high catalytic activity is attributed to the modification of the chemical environment on the catalyst surface and the optimized structural properties of the catalyst, including a large pore diameter, significant crystallite size, superior crystallinity, the highest proportion of oxygen vacancies, and a low density of basic sites. Notably, the 4%Cs loading confers a unique stabilization effect, effectively mitigating Cu leaching compared to other Cs loadings, thereby enhancing both catalyst stability and performance under reaction conditions. The XPS analysis reveals that the introduction of 4%Cs into the CuZnFe catalysts modifies the electronic environment, particularly around the Cu and O species, which could potentially influence the catalytic properties. Our investigation into the reaction mechanism indicates that the HA synthesis

experience a tandem pathway, incorporating both CO insertion and the formate pathway, with the latter being the predominant route. These results underscore the potential of the *x*Cs/CuZnFe catalyst in overcoming current challenges in ethanol and C_{2+} alcohols production through CO_2 hydrogenation, representing a notable advancement in the field of catalyst development.

CRediT authorship contribution statement

Andrii Kostyniuk: Writing – review & editing, Writing – original draft, Visualization, Validation, Software, Methodology, Investigation, Formal analysis, Data curation, Conceptualization. **Blaž Likozar:** Writing – review & editing, Supervision, Resources, Project administration, Methodology, Funding acquisition, Conceptualization.

Declaration of competing interest

The authors declare that they have no known competing financial interests or personal relationships that could have appeared to influence the work reported in this paper.

Acknowledgements

The authors express their gratitude for the financial support provided by the Slovenian Research Agency (ARIS) through the research Grant J7-4638 (Unlocking the selective catalytic conversion processes of CO_2 to ethanol – UliSess). The authors gratefully acknowledge Urška Kavčič for conducting the N_2 physisorption measurements, Dr. Anže Prašnikar for performing the SEM analysis, Mr. Edi Kranjc for the XRD analysis, and Dr. Goran Dražić for his assistance with TEM. Special thanks are extended to Dr. Janez Kovač for carrying out the XPS measurements and to Dr. Stanislav Iakushkin for performing the in situ DRIFTS measurements.

Appendix A. Supplementary data

Supplementary data to this article can be found online at https://doi.org/10.1016/j.cej.2025.166135.

Data availability

Data will be made available on request.

References

[1] A. Kostyniuk, B. Likozar, State-of-the-art advancements in the thermocatalytic conversion of CO2 into ethanol and higher alcohols: recent progress in catalyst development and reaction mechanisms, Chem. Eng. J. 503 (2025) 158467, https://doi.org/10.1016/j.cej.2024.158467.
[2] F. Zeng, C. Mebrahtu, X. Xi, L. Liao, J. Ren, J. Xie, H.J. Heeres, R. Palkovits, Catalysts design for higher alcohols synthesis by CO2 hydrogenation: trends and future perspectives, Appl. Catal. B Environ. 291 (2021) 120073, https://doi.org/10.1016/j.apcatb.2021.120073.
[3] S. De, A. Dokania, A. Ramirez, J. Gascon, Advances in the Design of Heterogeneous Catalysts and Thermocatalytic Processes for CO2 utilization, ACS Catal. 10 (2020) 14147–14185, https://doi.org/10.1021/acscatal.0c04273.
[4] I.C. Have, J.J.G. Kromwijk, M. Monai, F. Meirer, B.M. Weckhuysen, E.B. Sterk, Uncovering the reaction mechanism behind CoO as active phase for CO_2 hydrogenation, Nat. Commun. 13 (2022), https://doi.org/10.1038/s41467-022-27981-x.
[5] A. Kostyniuk, D. Bajec, B. Likozar, One-step synthesis of ethanol from glycerol in a gas phase packed bed reactor over hierarchical alkali-treated zeolite catalyst materials, Green Chem. 22 (2020) 753–765, https://doi.org/10.1039/c9gc03262b.
[6] W. Wang, C. Zeng, N. Tsubaki, Recent advancements and perspectives of the CO2 hydrogenation reaction, Green Carbon 1 (2023) 133–145, https://doi.org/10.1016/j.greenca.2023.10.003.
[7] S. Liu, Y. He, W. Fu, J. Chen, J. Ren, L. Liao, R. Sun, Z. Tang, C. Mebrahtu, F. Zeng, Hetero-site cobalt catalysts for higher alcohols synthesis by CO2 hydrogenation: a review, J. CO2 Util. 67 (2023) 102322, https://doi.org/10.1016/j.jcou.2022.102322.
[8] Y.A. Alli, P.O. Oladoye, O. Ejeromedoghene, O.M. Bankole, O.A. Alimi, E. O. Omotola, C.A. Olanrewaju, K. Philippot, A.S. Adeleye, A.S. Ogunlaja, Nanomaterials as catalysts for CO2 transformation into value-added products: a review, Sci. Total Environ. 868 (2023) 161547, https://doi.org/10.1016/j.scitotenv.2023.161547.
[9] J. Gao, S. Choo Sze Shiong, Y. Liu, Reduction of CO2 to chemicals and fuels: thermocatalysis versus electrocatalysis, Chem. Eng. J. 472 (2023) 145033, https://doi.org/10.1016/j.cej.2023.145033.
[10] S. Schemme, J.L. Breuer, R.C. Samsun, R. Peters, D. Stolten, Promising catalytic synthesis pathways towards higher alcohols as suitable transport fuels based on H2 and CO2, J. CO2 Util. 27 (2018) 223–237, https://doi.org/10.1016/j.jcou.2018.07.013.
[11] G. Prieto, Carbon dioxide hydrogenation into higher hydrocarbons and oxygenates: thermodynamic and kinetic bounds and Progress with heterogeneous and homogeneous catalysis, ChemSusChem 10 (2017) 1056–1070, https://doi.org/10.1002/cssc.201601591.
[12] R.P. Ye, J. Ding, W. Gong, M.D. Argyle, Q. Zhong, Y. Wang, C.K. Russell, Z. Xu, A. G. Russell, Q. Li, M. Fan, Y.G. Yao, CO2 hydrogenation to high-value products via heterogeneous catalysis, Nat. Commun. 10 (2019), https://doi.org/10.1038/s41467-019-13638-9.
[13] X. Li, M. Song, Y. Zhou, P. Zhou, D. Xu, T. Liu, X. Hong, Support-induced structural changes in CO2 hydrogenation to higher alcohols over metal/oxide catalysts, ChemCatChem (2024) e202301577, https://doi.org/10.1002/cctc.202301577.
[14] Y. He, F.H. Müller, R. Palkovits, F. Zeng, C. Mebrahtu, Tandem catalysis for CO2 conversion to higher alcohols: a review, Appl. Catal. B Environ. 345 (2024) 123663, https://doi.org/10.1016/j.apcatb.2023.123663.
[15] A.I. Latsiou, N.D. Charisiou, Z. Frontistis, A. Bansode, M.A. Goula, CO2 hydrogenation for the production of higher alcohols: trends in catalyst developments, challenges and opportunities, Catal. Today 420 (2023) 114179, https://doi.org/10.1016/j.cattod.2023.114179.
[16] X. Li, J. Ke, R. Li, P. Li, Q. Ma, T.S. Zhao, Research progress of hydrogenation of carbon dioxide to ethanol, Chem. Eng. Sci. 282 (2023) 119226, https://doi.org/10.1016/j.ces.2023.119226.
[17] Y. Sheng, M.V. Polynski, M.K. Eswaran, B. Zhang, A.M.H. Lim, L. Zhang, J. Jiang, W. Liu, S.M. Kozlov, A review of mechanistic insights into CO2 reduction to higher alcohols for rational catalyst design, Appl. Catal. B Environ. 343 (2024) 123550, https://doi.org/10.1016/j.apcatb.2023.123550.
[18] D. Xu, Y. Wang, M. Ding, X. Hong, G. Liu, S.C.E. Tsang, Advances in higher alcohol synthesis from CO2 hydrogenation, Chem 7 (2021) 849–881, https://doi.org/10.1016/j.chempr.2020.10.019.
[19] S.S. Ali, S.S. Ali, N. Tabassum, A review on CO2 hydrogenation to ethanol: reaction mechanism and experimental studies, J. Environ. Chem. Eng. 10 (2022) 106962, https://doi.org/10.1016/j.jece.2021.106962.
[20] Y.Z. Mao, F. Zha, H.F. Tian, X.H. Tang, Y. Chang, X.J. Guo, Progress in the thermocatalytic hydrogenation of CO2 to ethanol, J. Fuel Chem. Technol. 51 (2023) 1515–1528, https://doi.org/10.1016/S1872-5813(22)60065-3.
[21] S. Das, J. Pérez-Ramírez, J. Gong, N. Dewangan, K. Hidajat, B.C. Gates, S. Kawi, Core-shell structured catalysts for thermocatalytic, photocatalytic, and electrocatalytic conversion of CO2, Chem. Soc. Rev. 49 (2020) 2937–3004, https://doi.org/10.1039/c9cs00713j.
[22] S. Ji, F. Hong, D. Mao, Q. Guo, J. Yu, Enhanced ethanol synthesis from CO2 hydrogenation over Fe and Na CO-modified Rh/CeO2 catalysts, Chem. Eng. J. 495 (2024) 153633, https://doi.org/10.1016/j.cej.2024.153633.
[23] B. Ouyang, S. Xiong, Y. Zhang, B. Liu, J. Li, The study of morphology effect of Pt/Co3O4 catalysts for higher alcohol synthesis from CO2 hydrogenation, Appl. Catal. A Gen. 543 (2017) 189–195, https://doi.org/10.1016/j.apcata.2017.06.031.
[24] Y. Lou, F. Jiang, W. Zhu, L. Wang, T. Yao, S. Wang, B. Yang, B. Yang, Y. Zhu, X. Liu, CeO2 supported Pd dimers boosting CO2 hydrogenation to ethanol, Appl. Catal. B Environ. 291 (2021) 120122, https://doi.org/10.1016/j.apcatb.2021.120122.
[25] C. Zhou, A. Aitbekova, G. Liccardo, J. Oh, M. Stone, E.J. McShane, B. Werghi, S. Nathan, C. Song, J. Ciston, K. Bustillo, A.S. Hoffman, J. Hong, J. Perez-Aguilar, S. Bare, M. Cargnello, Steam-Assisted Selective CO2 Hydrogenation to Ethanol over Ru-In Catalysts, Angew. Chemie Int. Ed. (2024) e202406761. doi:https://doi.org/10.1002/anie.202406761.
[26] C. Yang, R. Mu, G. Wang, J. Song, H. Tian, Z.J. Zhao, J. Gong, Hydroxyl-mediated ethanol selectivity of CO2 hydrogenation, Chem. Sci. 10 (2019) 3161–3167, https://doi.org/10.1039/c8sc05608k.
[27] B. An, Z. Li, Y. Song, J. Zhang, L. Zeng, C. Wang, W. Lin, Cooperative copper centres in a metal–organic framework for selective conversion of CO2 to ethanol, Nat. Catal. 2 (2019) 709–717, https://doi.org/10.1038/s41929-019-0308-5.
[28] D. Xu, M. Ding, X. Hong, G. Liu, S.C.E. Tsang, Selective C2+ alcohol synthesis from direct CO2 hydrogenation over a Cs-promoted cu-Fe-Zn catalyst, ACS Catal. 10 (2020) 5250–5260, https://doi.org/10.1021/acscatal.0c01184.
[29] C. Yang, B. Wang, Y. Wen, M. Fan, Y. Jia, S. Zhou, W. Huang, Composition control of CuFeZn catalyst derived by PDA and its effect on synthesis of C2+ alcohols from CO2, Fuel 327 (2022) 125055, https://doi.org/10.1016/j.fuel.2022.125055.
[30] X. Wang, P.J. Ramírez, W. Liao, J.A. Rodriguez, P. Liu, Cesium-induced active sites for C-C coupling and ethanol synthesis from CO2 hydrogenation on cu/ZnO(0001) surfaces, J. Am. Chem. Soc. 143 (2021) 13103–13112, https://doi.org/10.1021/jacs.1c03940.
[31] S. Santanta, M.T.M. Koper, H.M. Alisson, L.H. Vieira, E.M. Assaf, M. Assaf, J. F. Gomes, Ethanol formation from CO2 hydrogenation at atmospheric pressure using cu catalysts: water as a key component, Appl. Catal. B Environ. 324 (2023) 122221, https://doi.org/10.1016/j.apcatb.2022.122221.
[32] C. Li, Q. Liu, D. Huang, J. Wang, Y. Xi, Z. Huang, F. Li, Catalytic tandem CO2 hydrogenation and Hydroformylation for high-yield synthesis of C2+ alcohols, ACS Catal. 15 (2025) 11440–11451, https://doi.org/10.1021/acscatal.5c02559.

[33] G.T. Jaya, R. Insyani, J. Park, A.F. Barus, M.G. Sibi, V. Ranaware, D. Verma, J. Kim, One-pot conversion of lignocellulosic biomass to ketones and aromatics over a multifunctional cu–Ru/ZSM-5 catalyst, Appl. Catal. B Environ. 312 (2022) 121368, https://doi.org/10.1016/j.apcatb.2022.121368.
[34] A. Kostyniuk, D. Bajec, P. Djinović, B. Likozar, Allyl alcohol production by gas phase conversion reactions of glycerol over bifunctional hierarchical zeolite-supported bi- and tri-metallic catalysts, Chem. Eng. J. 397 (2020) 125430, https://doi.org/10.1016/j.cej.2020.125430.
[35] P. Tian, G. Zhan, J. Tian, K.B. Tan, M. Guo, Y. Han, T. Fu, J. Huang, Q. Li, Direct CO2 hydrogenation to light olefins over ZnZrOx mixed with hierarchically hollow SAPO-34 with rice husk as green silicon source and template, Appl. Catal. B Environ. 315 (2022) 121572, https://doi.org/10.1016/j.apcatb.2022.121572.
[36] L. Ding, T. Shi, J. Gu, Y. Cui, Z. Zhang, C. Yang, T. Chen, M. Lin, P. Wang, N. Xue, L. Peng, X. Guo, Y. Zhu, Z. Chen, W. Ding, CO2 hydrogenation to ethanol over cu@Na-Beta, Chem 6 (2020) 2673–2689, https://doi.org/10.1016/j.chempr.2020.07.001.
[37] S. Zhou, Y. Wen, B. Wang, M. Fan, L. Ren, Z. Cui, W. Huang, J. Li, J. Guo, Regulation of CuFeZn catalysts by K3PO4 and its effect on CO2 hydrogenation to C2+ alcohols, Chem. Eng. J. 487 (2024) 150425, https://doi.org/10.1016/j.cej.2024.150425.
[38] A. Kostyniuk, D. Bajec, P. Djinović, B. Likozar, One-step synthesis of glycidol from glycerol in a gas-phase packed-bed continuous flow reactor over HZSM-5 zeolite catalysts modified by CsNO3, Chem. Eng. J. 394 (2020) 124945, https://doi.org/10.1016/j.cej.2020.124945.
[39] L.L. Ames, J.L. Wang, J.L. Margrave, The vaporization of cesium nitrate, Inorg. Nucl. Chem. Lett. 9 (1973) 1243–1246.
[40] I. Yanase, J. Konakawa, H. Kobayashi, Influence of cesium nitrate and heating rate on densification and microstructure of Cs-deficient pollucite sintered body, J. Am. Ceram. Soc. 89 (2006) 184–188, https://doi.org/10.1111/j.1551-2916.2005.00703.x.
[41] G. Singh, D. Khurana, T.S. Khan, I.K. Ghosh, B. Chowdhury, A.Y. Khodakov, A. Bordoloi, Insight into Mn enhanced short-chain olefins selectivity in CO2 hydrogenation over Na-CuFeO2 catalyst, Appl. Surf. Sci. 616 (2023) 156401, https://doi.org/10.1016/j.apsusc.2023.156401.
[42] D. Wang, Z. Xie, M.D. Porosoff, J.G. Chen, Recent advances in carbon dioxide hydrogenation to produce olefins and aromatics, Chem 7 (2021) 2277–2311, https://doi.org/10.1016/j.chempr.2021.02.024.
[43] M. Irshad, H.J. Chun, M.K. Khan, H. Jo, S.K. Kim, J. Kim, Synthesis of n-butanol-rich C3+ alcohols by direct CO2 hydrogenation over a stable cu–CO tandem catalyst, Appl. Catal. B Environ. 340 (2024) 123201, https://doi.org/10.1016/j.apcatb.2023.123201.
[44] K. Zheng, Y. Li, B. Liu, F. Jiang, Y. Xu, X. Liu, Ti-doped CeO2 stabilized single-atom rhodium catalyst for selective and stable CO2 hydrogenation to ethanol, Angew. Chem. Int. Ed. 61 (2022), https://doi.org/10.1002/anie.202210991.
[45] Q. Zhao, G. Fan, F. Li, Unique CuO –FeO interfaces in Cu-decorated Fe-based catalysts facilitating CO2 hydrogenation to higher hydrocarbons, Chem. Eng. J. 495 (2024) 153309, https://doi.org/10.1016/j.cej.2024.153309.
[46] Y. Wang, Y. Zhou, X. Zhang, M. Wang, T. Liu, J. Wei, G. Zhang, X. Hong, G. Liu, PdFe alloy-Fe5C2 interfaces for efficient CO2 hydrogenation to higher alcohols, Appl. Catal. B Environ. 345 (2024) 123691, https://doi.org/10.1016/j.apcatb.2024.123691.
[47] S. Zhang, C. Huang, Z. Shao, H. Zhou, J. Chen, L. Li, J. Lu, X. Liu, H. Luo, L. Xia, H. Wang, Y. Sun, Revealing and regulating the complex reaction mechanism of CO2 hydrogenation to higher alcohols on multifunctional tandem catalysts, ACS Catal. 13 (2023) 3055–3065, https://doi.org/10.1021/acscatal.2c06245.
[48] W. Xiang, S. Yasuda, M. Tonooka, W. Yang, K. Tsukamoto, G. Liu, G. Yang, W. Gao, N. Tsubaki, Potassium-driven pathway modulation in CO2 hydrogenation: tuning ethanol and liquid fuels synthesis over FeCuAl catalysts, Appl. Catal. B Environ. 369 (2025) 125157, https://doi.org/10.1016/j.apcatb.2025.125157.
[49] T. Ennaert, J. Geboers, E. Gobechiya, C.M. Courtin, M. Kurttepeli, K. Houthoofd, C. E.A. Kirschhock, P.C.M.M. Magusin, S. Bals, P.A. Jacobs, B.F. Sels, Conceptual frame rationalizing the self-stabilization of H-USY zeolites in hot liquid water, ACS Catal. 5 (2015) 754–768, https://doi.org/10.1021/cs501559s.
[50] B.L. Mojet, S.D. Ebbesen, L. Lefferts, Light at the interface: the potential of attenuated total reflection infrared spectroscopy for understanding heterogeneous catalysis in water, Chem. Soc. Rev. 39 (2010) 4643–4655, https://doi.org/10.1039/c0cs00014k.
[51] J. Wang, T. Wang, Y. Xi, G. Gao, P. Sun, F. Li, In-situ-formed potassium-modified nickel-zinc carbide boosts production of higher alcohols beyond CH4 in CO2 hydrogenation, Angew, Chemie 135 (2023) 1–10, https://doi.org/10.1002/ange.202311335.
[52] Y. Liu, X. Gong, R. He, Z. Han, J. Chen, B. Feng, X. Xu, A. Xing, R. Jin, P. Ren, B. Wang, Z.J. Wang, Stable three-dimensional macroporous Iron-foam catalyst for direct conversion of CO2 to olefins, ACS Catal. 14 (2024) 12425–12436, https://doi.org/10.1021/acscatal.4c03148.
[53] M. Irshad, H. Jo, S. Ahmed, W. Yoon, S. Ki, H. Chun, J. Kim, Tandem reductive hydroformylation: a mechanism for selective synthesis of straight-chain α-alcohols by CO2 hydrogenation, Appl. Catal. B Environ. Energy. 365 (2025) 124978, https://doi.org/10.1016/j.apcatb.2024.124978.
[54] R. Yao, B. Wu, Y. Yu, N. Liu, Q. Niu, C. Li, J. Wei, Q. Ge, Regulating the electronic property of iron catalysts for higher alcohols synthesis from CO2 hydrogenation, Appl. Catal. B Environ. 355 (2024) 124159, https://doi.org/10.1016/j.apcatb.2024.124159.
[55] Q. Gao, J. Xu, J. Wei, Y. Yu, Y. Sun, Q. Ge, Efficient synthesis of alcohols from syngas over Fe3O4 modified by P25 and ca, Appl. Catal. B Environ. Energy. 365 (2025) 124995.
[56] Q. Zhang, S. Wang, R. Geng, P. Wang, M. Dong, J. Wang, W. Fan, Hydrogenation of CO2 to higher alcohols on an efficient Cr-modified CuFe catalyst, Appl. Catal. B Environ. 337 (2023) 123013, https://doi.org/10.1016/j.apcatb.2023.123013.
[57] D. Xu, M. Ding, X. Hong, G. Liu, Mechanistic aspects of the role of K promotion on cu−Fe-based catalysts for higher alcohol synthesis from CO2 hydrogenation, ACS Catal. 10 (2020) 14516–14526, https://doi.org/10.1021/acscatal.0c03575.
[58] H. Wang, S. Fan, S. Guo, S. Wang, Z. Qin, M. Dong, H. Zhu, W. Fan, J. Wang, Selective conversion of CO2 to isobutane- enriched C4 alkanes over InZrOx-Beta composite catalyst, Nat. Commun. (2023) 1–14, https://doi.org/10.1038/s41467-023-38336-5.
[59] J. Sun, Q. Cai, Y. Wan, S. Wan, L. Wang, J. Lin, D. Mei, Y. Wang, Promotional effects of cesium promoter on higher alcohol synthesis from syngas over cesium-promoted cu/ZnO/Al2O3 catalysts, ACS Catal. 6 (2016) 5771–5785, https://doi.org/10.1021/acscatal.6b00935.